Geophysical Journal International

Geophys. J. Int. (2023) **235,** 1778–1797
Advance Access publication 2023 August 16
GJI Rock and Mineral Physics, Rheology

https://doi.org/10.1093/gji/ggad322

Fabric controls fault stability in serpentinite gouges

G. Pozzi,[1] C. Collettini,[2,1] M. M. Scuderi,[2] T. Tesei,[3] C. Marone,[2] A. Amodio[1] and M. Cocco[1]

[1]*Istituto Nazionale Di Geofisica e Vulcanologia (INGV), Rome* 00143*, Italy E-mail: giacomo.pozzi@ingv.it*
[2]*Dipartimento di Scienze della Terra, La Sapienza University of Rome, Rome* 00185*, Italy*
[3]*Dipartimento di Geoscienze, University of Padua, Padova* 35131*, Italy*

Accepted 2023 August 7. Received 2023 July 21; in original form 2023 May 15

SUMMARY

Serpentinites are polymineralic rocks distributed almost ubiquitously across the globe in active tectonic regions. Magnetite-rich serpentinites are found in the low-strain domains of serpentinite shear zones, which act as potential sites of nucleation of unstable slip. To assess the potential of earthquake nucleation in these materials, we investigate the link between mechanical properties and fabric of these rocks through a suite of laboratory shear experiments. Our experiments were done at room temperature and cover a range of normal stress and slip velocity from 25 to 100 MPa and 0.3 to 300 μm s^{-1}, respectively. We show that magnetite-rich serpentinites are ideal materials since they display strong sensitivity to the loading rate and are susceptible to nucleation of unstable slip, especially at low forcing slip velocities. We also aim at the integration of mechanical and microstructural results to describe the underlying mechanisms that produce the macroscopic behaviour. We show that mineralogical composition and mineral structure dictates the coexistence of two deformation mechanisms leading to stable and unstable slip. The weakness of phyllosilicates allows for creep during the interseismic phase of the laboratory seismic cycle while favouring the restoration of a load-bearing granular framework, responsible of the nucleation of unstable events. During dynamic slip, fault zone shear fabric determines the mode of slip, producing either asymmetric or Gaussian slip time functions for either fast or slow events. We report rate/state friction parameters and integrate our mechanical data with microstructural observations to shed light on the mechanisms dictating the complexity of laboratory earthquakes. We show that mineralogical and fabric heterogeneities control fault slip behaviour.

Key words: Friction; Earthquake dynamics; Rheology and friction of fault zones; Mechanics, theory and modelling; Microstructures; Experimental rock deformation.

1 INTRODUCTION

Faults accommodate tectonic deformation in the upper crust through a spectrum of slip behaviours that range from stable sliding to fast slip during earthquakes (e.g. Peng & Gomberg 2010; Leeman *et al.* 2016; Harris 2017; Scholz 2019). This includes creep events and strain transients, slow earthquakes, low frequency earthquakes, tectonic fault tremor and post-seismic afterslip. Complex modes of fault slip have been interpreted in terms of frictional, rheological and geometrical heterogeneity within fault zones (Marone & Richardson 2010; Skarbek *et al.* 2012; Saffer & Wallace 2015; among many others) and laboratory studies have shown that shear fabric evolution in fault zones plays a key role in determining fault strength, rheology and slip behaviour (e.g. Holdsworth 2004; Collettini *et al.* 2009; Schleicher *et al.* 2010). Similar inferences have been deduced from the geological record, which suggests that a spectrum of fault slip modes occur within thick, mature faults that include broad damage zones and localized principal slip zones (e.g. Fagereng & Sibson 2010; Scholz 2019).

Fault slip behaviour and seismogenic potential are determined by the fault zone mineralogy and properties of the wear materials within the fault core (Scholz 2019). The wear materials, known as cataclasites and fault gouges, are typically heterogeneous mixtures of the wall rock of different age and origin, with shear fabric of varying intensity depending on the dominant rock type (Sibson 1977). From this heterogeneity emerges one key to understanding the complex slip behaviour of a variety of 'weak' faults, which do not follow Byerlee's rule (Holdsworth 2004; Collettini *et al.* 2021). Fault gouges are typically fine-grained, foliated rocks composed of both granular (e.g. quartz, feldspars, etc.) and platy (phyllosilicate) materials. These two main mineral categories are distinct for their geometrical properties and fabric intensity (e.g. Sibson 1977) and

show an almost antipodal mechanical behaviour, being—in most of the studied cases—respectively strong and weak to shear motion (e.g. Byerlee 1978; Ikari *et al.* 2011; Collettini *et al.* 2021). Several works demonstrated that the frictional strength of these gouge materials is not solely a material-dependent characteristic but also the result of the spatial arrangement and optimal orientation of their geometrical attributes and rheological properties, which together define the fabric of the rock. If platy minerals are favourably oriented to shear motion, the rock has a well-developed fabric, which favours weakness (among many, Handy 1990; Wintsch *et al.* 1995; Collettini *et al.* 2009; Niemeijer *et al.* 2010; Tesei *et al.* 2014; Vannucchi 2019; Bedford *et al.* 2022). Laboratory work has documented the role of fabric in promoting weakness, but it appears that natural faults with intense fabrics are even weaker in some cases.

Phyllosilicates are common minerals in faults since they are the primary component of sedimentary and igneous rocks, and are easily formed during metamorphism, metasomatism and supergene alteration of silica-rich rocks. Deformation along fault systems promotes their formation by increasing the surface of minerals exposed to alteration and by enhancing fluid flow along the fault core where fresh surface area is produced continually during brecciation and comminution during fault motion. This almost ubiquitous presence of phyllosilicate minerals has motivated much research on natural and analogue mixtures of granular and platy materials (e.g. Bos & Spiers 2001; Tembe *et al.* 2010; Moore *et al.* 2011; Behnsen and Faulkner, 2012; Ikari *et al.* 2011, 2013; Haines *et al.* 2013; Tesei *et al.* 2014; Giorgetti *et al.* 2015; Ruggieri *et al.* 2021).

As much as heterogeneity characterizes the mineralogy of such rocks, their frictional properties are not trivially predicted and are strongly affected by modal distribution, fabric and boundary conditions (e.g. water saturation, temperature). Understanding the link that interconnects these features with the rheological properties of granular-phyllosilicate fault materials is important for the understanding of fault slip (phenomenological and quantitative) behaviour.

One key example is the velocity dependence of constitutive parameters in the rate- and state-dependent friction laws (a, b and D_c) documented in granular-phyllosilicate mixtures (Saffer *et al.* 2003; Niemeijer & Spiers 2007; Ikari *et al.* 2011, 2013; den Hartog & Spiers 2013; Ruggieri *et al.* 2021; Scuderi *et al.* 2022; Volpe *et al.* 2022a), with direct implications on earthquake nucleation and its theoretical modelling (e.g. Leeman *et al.* 2018; Im *et al.* 2020). Despite recent progress on fault frictional characterization, there is still a lack of understanding on the connection between velocity-dependent constitutive parameters and mineralogy and fabric. We explore in this work the link existing between mineralogy, fabric and rate- and state-dependent frictional properties by choosing a relevant natural material composed by a mixture of phyllosilicates and strong granular materials: serpentine rocks, which are an emblematic example of such heterogeneity.

Serpentinites are polymineralic rocks distributed almost ubiquitously across the globe in active tectonic regions (e.g. Guillot *et al.* 2015). They are the result of hydrous metamorphism of peridotites, which results in a rock composed mainly by serpentine group minerals (antigorite, lizardite and chrysotile) and magnetite, with minor pyroxene, talc and other accessories. The main component, serpentine polymorphs, are phyllosilicates with typically small values of friction coefficients (apart from the high-grade polymorph, the antigorite) that deform mainly by frictional sliding (Reinen *et al.* 1994; Moore *et al.* 1996, 1997; Escartin *et al.* 1997; Moore & Rymer 2007; Tesei *et al.* 2018; Scuderi & Carpenter 2022). Magnetite, instead, is a rheologically strong granular material, with friction coefficients close to Byerlee's values (Byerlee 1978; Österle *et al.* 2014). We used natural samples of lizardite–magnetite rich serpentinites cropping-out in a thin nappe of the Elba Island (Italy), locality Monte Fico (Keller & Pialli 1990). The rocks, already characterized with XRD and TEM analysis in previous work by Tesei *et al.* (2018), were deformed in a set of shear laboratory experiments. We observed a systematic change of mechanical properties and fault slip behaviours with the variation of the sliding velocity that we interpret to be the result of the time-dependent arrangement of grains within a heterogeneous experimental fault architecture.

2 EXPERIMENTAL SETUP AND METHODOLOGY

Experiments were conducted on serpentinite rocks collected from low strain domains of the Monte Fico thrust zone, in Elba Island Italy. Samples were powdered to form synthetic fault gouge and sieved below 125 μm. This serpentinite consists dominantly of lizardite (constrained with TEM analysis, Tesei *et al.* 2018), magnetite and minor diopside. The relative abundance of magnetite (>7 per cent volume) is retrieved using ImageJ (Schneider *et al.* 2012) by thresholding back-scattered SEM images. Powders were tested at room temperature (25–27 °C) and room humidity (30–40 per cent) in the bi-triaxial shear apparatus BRAVA in double direct shear (DDS) configuration (Collettini *et al.* 2014, Fig. S1). The assembly consists of a central forcing block sandwiched between two stationary side blocks that confine two synthetic fault zones. The faults are each initially 5 mm in thickness, prior to load and shear. When mounted in the deformation apparatus, normal stress is applied perpendicular to the layers by one ram while shear stress is applied by the other ram. Fault zone shear is imposed by the central block of the DDS assembly with a stiffness of $k = 0.928$ kN μm^{-1}. Grooves engraved on the forcing blocks in contact with the sample ensure that shear occurs within the fault zone rather than at its boundary. The relative motion of the rams is measured close to the hydraulic pistons by LVDTS with a precision of ±0.1 μm. The vertical motion and displacement rate measured at this position are referred to as 'loading point' displacement and velocity (LPV), respectively. We also measure shear displacement directly across the fault using an additional LVDT (Fig. S1b). We measure forces using calibrated load cells and convert these to shear and normal stress on the fault surfaces using the fault area which is 50 by 50 mm.

Experiments for standard characterization of frictional parameters were run at four normal stresses, $\sigma_N = 25$, 50, 75 and 100 MPa, using two experimental protocols. The first consisted of four stages (Fig. 1a). Samples were initially brought to target normal stress and allowed to compact for ∼15′. During this stage, the initial high-porosity gouge layers decrease their total thickness by 4–5 mm (Fig. S3a). After compaction, samples were sheared at constant velocity of 10 μm s^{-1} for a total displacement of ∼1 cm to attain near steady-state friction coefficients (run-in stage, Fig. 1a). Subsequently, the shear motion was cyclically stopped and re-applied in a series of slide-hold-slide (SHS, Fig. 1a) tests. Hold times were incremented according to the sequence 1, 3, 10, 30, 100, 300, 1000 and 3000 s. Between each hold the sample was sheared at constant velocity of 10 μm s^{-1} for a total slip of 500 μm. Afterwards, two sequences of velocity step (Fig. 1a) tests were performed to assess velocity and state dependence of friction. During velocity step tests

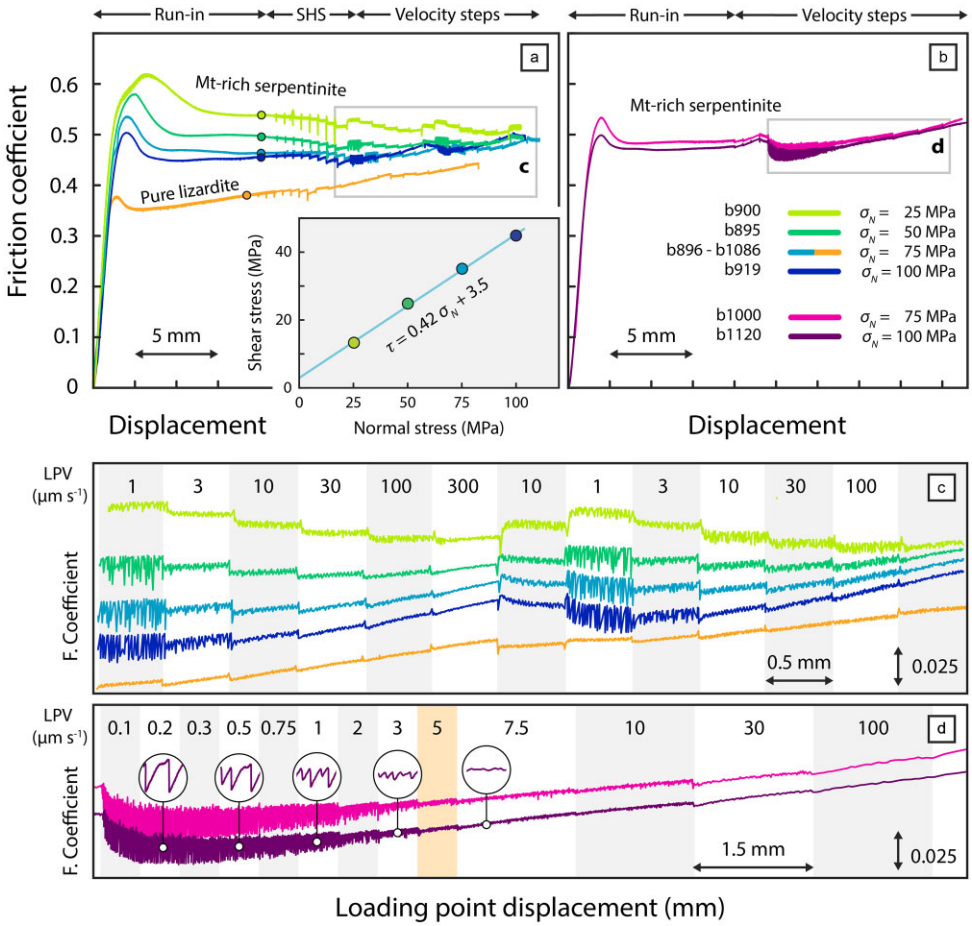

Figure 1 Mechanical data: (a) Evolution of the apparent friction coefficient obtained with Type I experiments with a run-in, slide-hold-slide (SHS) test and two consecutive velocity step tests. The grey frame shows the velocity step tests highlighted in panel (c). The grey inset shows the steady-state shear stress values (coloured dots) plotted in a Mohr diagram. The best-fitting linear equation is reported in the inset. (b) Friction during Type II experiments with a run-in and velocity steps. The grey frame shows the data zoomed in panel (d). (c) Friction evolution during velocity step tests from panel (a). Note the modest but evident strength increase due to slip hardening at high normal stress for magnetite-rich serpentinite and for lizardite. σ_N and τ are the normal and shear stress, respectively. See Table 1 for experiment conditions and fault gouge materials. (d) Friction evolution and frictional instabilities during Type II experiments. Zooms are shown for a few cases to highlight unstable stick-slip events. Loading point velocities (LPV) are given in the top margins of panels (c) and (d). Orange shaded area in panel (d) indicates the transition from unstable to stable sliding, which occurs at LPV = 5 μm s^{-1}.

the sliding velocity was changed every 500 μm with the following LPVs: 10, 1, 3, 10, 30, 100 and 300 μm s^{-1}. The same protocol was used for a single test performed at $\sigma_N = 75$ MPa on pure lizardite gouge (the same selected by Tesei *et al.* 2018).

Two additional tests were performed with the second protocol at 75 and 100 MPa with the aim of characterizing the frictional stability of the experimental fault in a wider range of sliding velocities. These tests (Fig. 1b) consisted of a run-in phase (LPV = 10 μm s^{-1} for a total slip of 10 mm), followed by velocity stepping from 10 to 300 μm s^{-1}, and a sequence of velocity steps with the following LPVs: 0.1, 0.2, 0.3, 0.5, 0.75, 1, 2, 3, 5, 7.5, 10, 30, 100 and 300 μm s^{-1}. For the second sequence, velocity was kept constant for 500 μm at each velocity up to 5 μm s^{-1}, 1500 μm for all the others. The sampling frequency during these velocity steps is 100 Hz. We used an iterative, non-linear least squares procedure to measure the friction constitutive parameters (using the module 'RawPy' for Python; https://github.com/marcoscuderi/rawPy). Table 1 provides the gouge compositions, conditions and results for our first suite of experiments.

3 EXPERIMENTAL RESULTS

3.1. Friction curves and fault stability

Magnetite-rich serpentinite gouges display different values of the friction coefficient at the end of the run-in phase (dots in Fig. 1a). The friction coefficient, defined as the ratio between shear and normal stress, decreases with increasing normal stress with steady-state values of $\mu = 0.54$, 0.50, 0.47 and 0.45 for $\sigma_N = 25$, 50, 75 and 100 MPa, respectively (measured at the coloured dots in Fig. 1a). In a Mohr space (Fig. 1a, grey inset), the steady-state values of shear stress (measured at the same location of the steady-state friction coefficient) align according to a linear criterion. The slope of this fit corresponds to the internal friction coefficient $\mu_I = 0.42$, which is not normal stress dependent, and the intercept is a non-zero cohesion $c = 3.5$ MPa. Marked frictional instability with stick-slip events occurs at normal stresses equal or larger than 50 MPa and only for LPVs lower than 10 μm s^{-1} (Fig. 1c), while for higher LPVs, or lower stress, the sample undergoes stable sliding. This

Table 1 Experimental data: experimental conditions and retrieved mechanical data of the first experimental protocol. The two columns of the (a–b) and D_c parameters correspond to the two consecutive velocity-step tests.

Material	Exp. code	Normal stress	Friction coefficient	Rate and state parameters					Frictional healing rate	Creep relaxation
		σ_N (MPa)	μ	$V_0 \rightarrow V$ (μm s^{-1})	(a–b)		D_c (μm)		β ($\Delta\mu$ log^{-1} s)	
Magnetite-rich serpentinite	b900	25	0.54	0.3 → 1	−0.0057	−0.0060	75.4	55.5	0.0015	−0.0091
				1 → 3	−0.0050	−0.0050	66.3	85.3		
				3 → 10	−0.0044	−0.0048	76.7	49.9		
				30 → 100	−0.0024	−0.0028	6.7	18.6		
				100 → 300	−0.0014	−0.0016	11.1	14.4		
	b895	50	0.50	<10	Unstable				−0.0006	−0.0048
				10 → 30	−0.0033	−0.0036	2.5	2.8		
				30 → 100	−0.0022	−0.0024	4.8	2.6		
				100 → 300	−0.0013	−0.0015	5.4	7.1		
	b896	75	0.47	<10	Unstable				−0.0018	−0.0037
				10 → 30	−0.0030	−0.0027	2.5	3.1		
				30 → 100	−0.0021	−0.0021	4.2	3.7		
				100 → 300	−0.0013	−0.0014	5.9	6.6		
	b919	100	0.45	<10	Unstable				−0.0022	−0.0034
				10 → 30	−0.0021	−0.0021	2.7	2.4		
				30 → 100	−0.0014	-0.0015	4.0	2.7		
				100 → 300	−0.0010	−0.0006	6.4	5.1		
Lizardite	b1086	75	0.38	0.3 → 1	−0.0021	−0.0017	1.5	3.6	−0.0026	−0.0043
				1 → 3	−0.0022	−0.0013	3.8	4.7		
				3 → 10	−0.0009	−0.0003	3.2	5.2		
				30 → 100	−0.0001	0.0003	6.1	4.2		
				100 → 300	0.0015	0.0019	2.8	6.5		

is clearly observed in the second set of experiments at high normal stress (75 and 100 MPa) and for a broader range of LPVs (as low as 0.1 μm s^{-1}) shown in Figs 1(b) and (d). The circles in panel (d) show a zoom of stick-slip events observed at different values of LPV, pointing out the effect of LPV on frictional instabilities. The magnitude of stress drops during sequences of stick-slip events decreases with increasing LPV, as qualitatively shown in the insets of Fig. 1(d). A detailed analysis of stick-slip events and their properties is presented in Section 5. The results for faults composed of pure lizardite (Fig. 1a) at $\sigma_N = 75$ MPa emphasizes the different frictional behaviour of this material. Lizardite shows a constant slip hardening behaviour, with values of $\mu =$ 0.38 at the end of the run-in stage and, notably, no instabilities at any explored values of LPV. At $\sigma_N \geq 50$ MPa magnetite-rich serpentinite gouges display a slip hardening behaviour when sliding velocities are higher than 10 μm s^{-1}. This effect, which is clearly evident when comparing the run-in curve with the following velocity step section, is enhanced at higher stresses (Fig. 1c). Different slip hardening does not seem related to differences in layer compaction as the total layer thickness decreases (after the compaction stage, Fig. S3a) of comparable amounts in all experiments, due to geometrical thinning. Furthermore, the variation of layer thickness with vertical displacement (Fig. S3b) is identical for all investigated stresses during the first experimental protocol (Fig. 1a).

The experiments of Fig. 1 show that, despite the dominant stable frictional response, stick-slip instabilities can be generated in serpentinite gouge depending on normal stress conditions and load point velocities (LPV).

3.2. Rate and state parameters

Stemming from the analysis of the spring slider motion, the mechanical data are successfully analysed within the 'rate and state friction' (RSF) framework (e.g. Dieterich 1979; Ruina 1983; Marone 1998), where unstable sliding may emerge if: (i) the material weakens with increasing sliding velocity and (ii) the stiffness of the loading system (k^*) is lower than a critical stiffness (k_c^*), described by eq. (1) (Gu *et al.* 1984; Baumberger 1994).

$$k^* < k_c^* = \frac{-(a-b)}{D_c}\sigma_N. \quad (1)$$

The dimensionless term (a–b) quantifies the steady state frictional response to a change in sliding velocity (i.e. rate) while D_c (critical slip distance) has the dimension of a length and represents the characteristic slip required to achieve steady state after a change in load point velocity. For simplicity, we will use throughout the text k and k_c, which are the same values k^* and k_c^* normalized by the normal stress. The variables (a–b) and D_c are measured by inverting the mechanical data obtained during velocity stepping by using eqs (2), (3) and (4). Eq. (2) describes the effect of slip rate V and frictional state θ on friction:

$$\mu = \mu_0 + a \log_{10}\left(\frac{V}{V_0}\right) + b \log_{10}\left(\frac{V_0\theta}{D_c}\right), \quad (2)$$

where μ_0 is the steady-state friction at the reference sliding velocity V_0, V is the sliding velocity after the step, θ is the state variable, with dimensions of time, often thought of as the contact junction lifetime (Rabinowizc 1951). D_c can be interpreted as the length scale parameter controlling the evolution of the state variable. Eq. (2) is

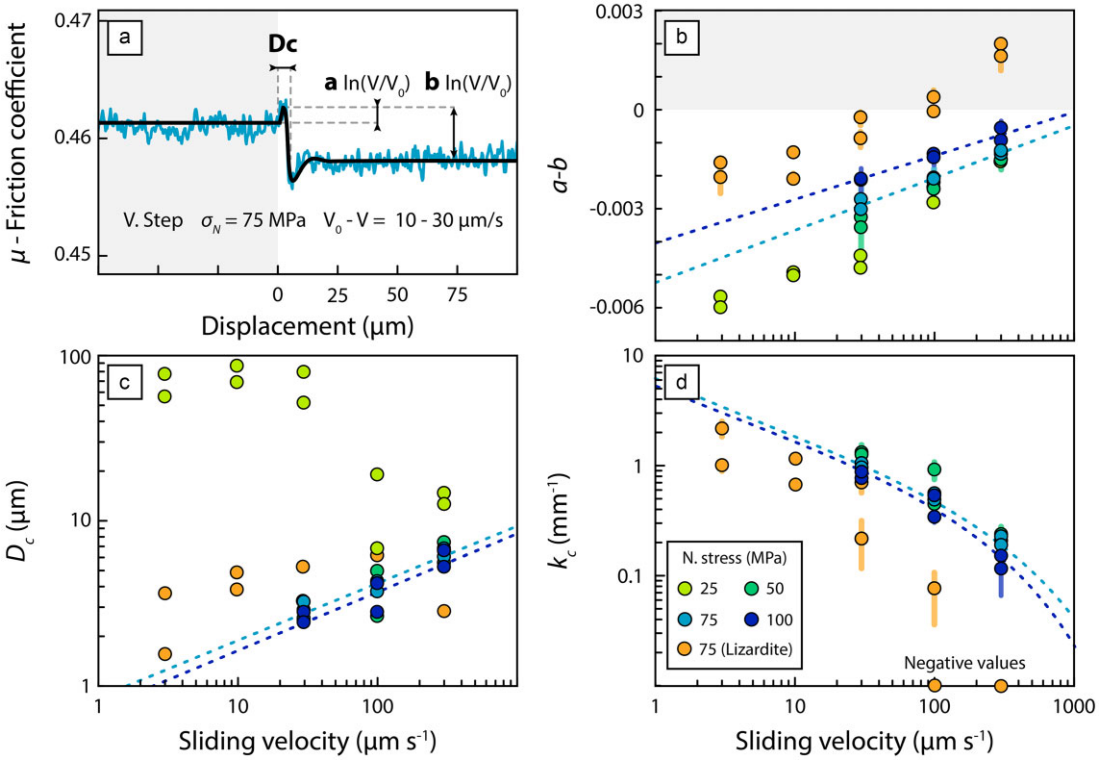

Figure 2 RSF parameters: (a) example of friction data (blue) and RSF model fit (black) for (a) velocity step test. Panels (b), (c) and (d) show values of (a–b), D_c and K_c as a function of sliding velocity, respectively. Best-fitting curves (dashed lines) are shown for experiments at $\sigma_N = 75$ and 100 MPa (see colour key in panel (d). Dashed curves in panel (d) are from eq. (5). Error bars in all panels correspond to one standard deviation, not visible if smaller than the symbol.

Table 2 Best-linear fit of rate- and state-dependent parameters

Stress (MPa)	Variable	Space	Slope (m)	Intercept (q)	R^2
75	a–b	Lin–Log	0.0016	−0.0052	0.9807
	D_c	Log–Log	0.3448	−6.0713	0.9285
100	a–b	Lin–Log	0.0013	−0.0041	0.9599
	D_c	Log–Log	0.3460	−6.1258	0.8207

combined with a friction state evolution law, and we use the law proposed by Ruina (1983):

$$\frac{\mathrm{d}\theta}{\mathrm{d}t} = -V\frac{\theta}{D_c}\log_{10}\left(V\frac{\theta}{D_c}\right). \quad (3)$$

Note that at steady state, frictional state is given by the ratio D_c/V. To solve for friction evolution after a perturbation in sliding velocity, one must account for elastic interaction between the fault zone and its surroundings. In laboratory experiments it is common to use a 1-D system as:

$$\frac{\mathrm{d}\mu}{\mathrm{d}t} = k\,(\mathrm{LPV} - V)\,, \quad (4)$$

where k is the normalized loading stiffness and LPV is the load point velocity. We invert for the RSF parameters a, b and D_c using an iterative, least-square non-linear procedure to solve eqs (3) and (4) simultaneously, while using eq. (2) to relate friction and state. We use a fifth-order Runge–Kutta integration technique with adaptive step-size control (e.g. Blanpied *et al.* 1998; Saffer & Marone 2003). Fig. 2(a) shows an example of an inverted friction evolution following a velocity step, numerical values are reported in Table 1.

Values of (a–b) in magnetite-rich serpentinite gouges are negative for all selected slip velocities (Fig. 2b) and display direct linear dependency to the logarithm of the sliding velocity (Fig. 2b). Lizardite powders produce similar dependency to velocity, even though the negative (a–b) values become neutral to positive at velocities ≥100 μm s^{-1}. Values of D_c for serpentinite are rather small (below 10 μm), linearly dependent on sliding velocity (V) in a log–log space and seemingly independent of the normal stress (Fig. 2c). The experiment at $\sigma_N = 25$ MPa represents an exception with values as high as 90 μm, especially at low slip velocities (<100 μm s^{-1}). This result corroborates the difference in frictional behaviour shown in Fig. 1 for low values of normal stress. The critical slip distance of lizardite is less sensitive to velocity but is comparable to that of magnetite-rich serpentinite. k_c as defined in eq. (1) has values in a range between 2 and 0.1 mm^{-1} (Fig. 2d), with a few negative values for lizardite due to the positive values of (a–b) (Fig. 2b).

Given the evident dependency on sliding velocity for both (a–b) and D_c parameters, we analyse best-fitting values of rate- and state-dependent parameters to investigate the stability of the experimental fault. For this task, we have analysed the data from the second type of experiments performed at $\sigma_N = 75$ and 100 MPa and with the long sequence of velocity steps (Figs 1b and d). The regression lines of rate and state data are shown in Figs 2(b) and (c) (dashed lines). Best-fitting values are reported in Table 2. Following eq. (1), k_c values can be also estimated through the ratio of the two inferred best-fitting lines for (a–b) and D_c parameters (dashed lines in Figs 2b

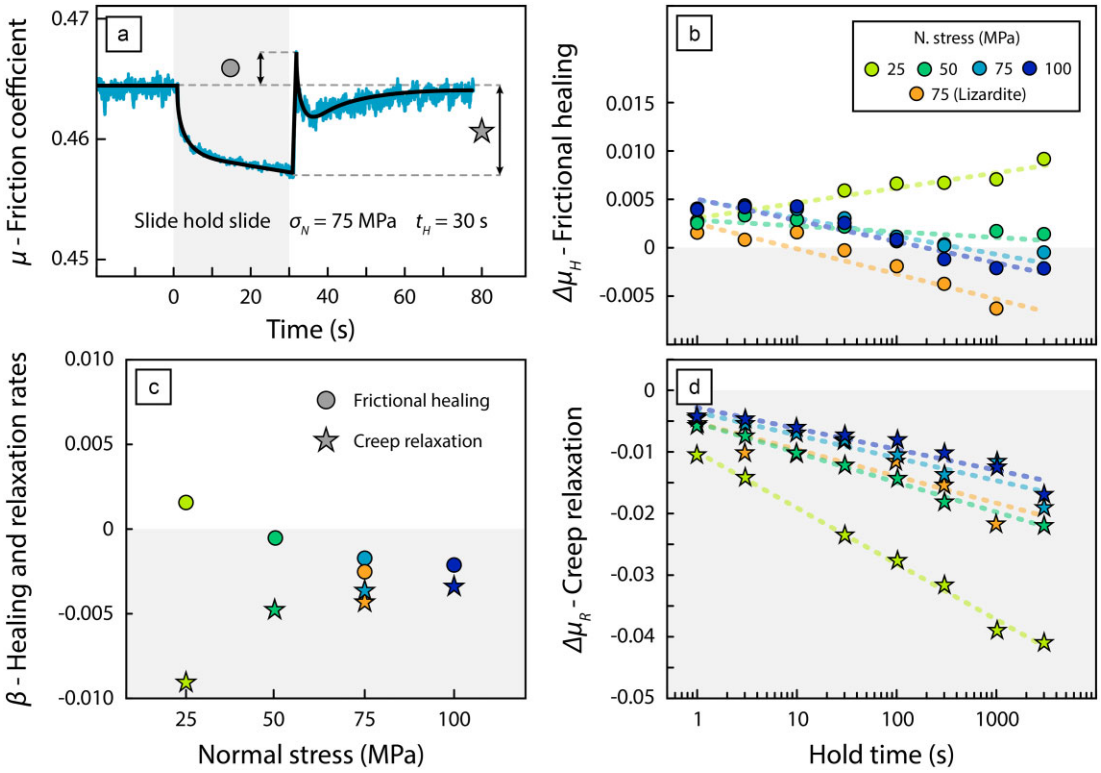

Figure 3 Frictional healing: (a) Data showing how we measure frictional healing $\Delta\mu_H$ (see circles) and creep relaxation $\Delta\mu_R$ (see stars) during a slide-hold-slide test (hold time shaded in grey); (b) frictional healing and (d) creep relaxation values obtained at increasing hold times, with dashed lines representing the linear fit (lin–log space) whose slopes, the healing and relaxation rates (β), are reported in panel (c).

and c, respectively), as defined in eq. (5):

$$k_c = -\frac{m_{a-b}\log_{10}(V) + q_{a-b}}{10^{(m_{D_c}\log_{10}(V)+q_{D_c})}}, \quad (5)$$

where m and q indicate the slope and the intercept of the linear regression lines for (a–b) and D_c parameters, retrieved in lin–log and log–log scales, respectively.

By using the values of Table 2 in eq. (5), we observe a nearly log–log linear inverse dependency of k_c on sliding velocity up to 30 μm s^{-1} (Fig. 2d) and minor deviations for the different imposed normal stress values. Then, k_c rapidly decreases to low values, more than one order of magnitude lower than normalized machine stiffness, which is above 3 mm^{-1} for the stresses here considered. This clearly represents the k_c dependency on V, consistent with previous works (e.g. Baumberger *et al.* 1994; Leeman *et al.* 2016).

The comparison of friction evolution during velocity step experiments shows that, at σ_N equal or higher than 50 MPa, friction does not achieve steady state conditions after a velocity step (Fig. 1c), even though D_c is on the scale of few micrometres (Fig. 2c). This is especially evident with increasing LPVs and normal stress (note the severe hardening of serpentinite at σ_N = 75 and 100 MPa, Fig. 1d), and when the tested gouge is pure lizardite (Fig. 1c). The dependence of this slip hardening on loading velocity (LPV) and normal stress suggests that the gouge layer has a complex response to a change in velocity. We interpret the observed slip hardening in terms of an additional slow (long-term) evolutive effect affecting the bulk response to the change in velocity. This second evolutive effect is slower than the response to the velocity step, which is expected to be governed by the evolution of the state variable as predicted by eq. (3). In other words, it represents a deviation from the steady state response to a velocity step predicted by rate- and state-dependent friction laws with a single state variable. We point out that the friction evolution with slip depicted in Fig. 2(a), nicely modelled with rate- and state-dependent friction through eqs (2) and (3), only shows the instantaneous response as evidenced by the small slip values, and that the observed slip hardening is occurring at longer time scales. This aspect will not be analysed in terms of rate and state friction in the main text. The reader is referred to Supplementary section SII and Fig. S2(a) for highlights on this matter.

3.3. Time dependent frictional healing

Slide-hold-slide tests (Fig. 1a) are used to estimate time-dependent frictional healing and assess RSF parameters (e.g. Marone 1998). We measure frictional healing values $\Delta\mu_H$ as the difference between the steady state friction prior to the hold and the peak friction measured upon reshear after slip is interrupted for a specific (hold) time (circle symbol, Fig. 3a). The linear fit of these values (Fig. 3b) as function of the logarithm of hold time provides the relative values of healing rate (β, circles in Fig. 3c). Numerical values are reported in Table 1.

The healing rates of magnetite-rich serpentinite gouges are negative for investigated normal stresses except for σ_N = 25 MPa. β values decrease monotonically with increasing normal stress. Lizardite gouges at σ_N = 75 MPa show null to negative frictional healing with negative β values, with both β and $\Delta\mu_H$ values slightly lower than that of serpentinite (Figs 3b and d). Overall, healing rates are consistent with those documented in phyllosilicate-rich, weak lithologies (e.g. Carpenter *et al.* 2011; Carpenter *et al.* 2016; Tesei *et al.* 2012; Collettini *et al.* 2021; Scuderi & Carpenter 2022).

The absolute values of creep relaxation rates are low (<0.01 $\log^{-1}$ s), typical of phyllosilicate-rich materials (Carpenter *et al.* 2016). Opposite to the frictional healing, these values decrease with normal stresses, with the highest values observed in magnetite-rich serpentinite at $\sigma_N = 25$ MPa. The creep relaxation rate of lizardite at $\sigma_N = 75$ MPa is very similar to that of magnetite-rich serpentinite at the same normal stress.

The analysis of frictional healing and creep relaxation, similarly to the rate and state analysis, evidences the separation of frictional behaviour that characterizes magnetite-rich serpentinites at low normal stress as well as pure lizardite. If, on one hand, we infer the role of the lizardite fraction in the processes that underlay creep relaxation and the negative healing rates (similar for both materials), the higher $\Delta\mu_H$ values of magnetite-rich gouges calls for investigation of the role of fabric heterogeneity.

One aspect that should also be noted from friction curves is that, when hold times become longer than 10 s, the effect of creep relaxation outlasts the recovery of steady state friction during slides (Fig. 1a, enlarged in Fig. S2a). This effect is opposite—even if underlying mechanisms may share the same nature—to the slip hardening originating from velocity stepping. This leads the experimental fault to a 'relaxed' state, which requires long timescales of reset. Again, we do not discuss in detail this aspect in the main text and refer the reader to the Supplementary section SII and Figs S2 and S4.

4 ANALYSIS OF STICK-SLIP EVENTS

Our data show that laboratory-scale earthquake (lab-quakes) parameters for magnetite-rich serpentinites vary systematically with load point velocity (LPV). Frictional sliding is unstable at lower slip velocity and becomes stable at higher LPV (Fig. 1). This transition is reflected in RSF parameters. We observe enhanced velocity weakening behaviour (lower a–b) and smaller values of D_c for lower LPV, which favours stick-slip instabilities at velocities of $\leq$5 μm s^{-1} (Figs 1 and 2). The transition is consistent with the fact that the frictional weakening rate with slip (k_c) is higher at lower LPV, and thus instability occurs because the condition $k < k_c$ is met, where k is loading system stiffness. We observe larger stress drops for lower values of LPV, as expected based on the variation of k_c with LPV (Fig. 2). However, the simple analysis of RSF and the stability condition cannot account for all of the phenomenology we observe (e.g. Figs 1b and d). We show in the following that, despite similar k_c values are inferred at both $\sigma_N = 75$ and 100 MPa (Fig. 1d), stick-slip events are characterized by different mechanical properties such as the dynamic stress drop, peak slip velocity and the symmetry of slip velocity time histories (Fig. S5 for a schematic of the measured values).

4.1. Dynamic slip velocity and stress drop

We show in Fig. 4 the slip velocity and stress drop time histories of the stick-slip events of experiments reported in Fig. 1(b). The slip velocity is obtained by differentiating the fault displacement in time and we refer to its evolution in time as a slip velocity function (SVF). The SVF curves are illustrated in Fig. 4(a) for each loading point velocity and for two values of fault normal stress. These velocities represent the average sliding behaviour for the laboratory fault (considered as a point source) and can be analysed similarly to the source-time functions inferred from 2-D dynamic rupture modelling or kinematic and pseudo-dynamic modelling (Yoffe 1951; Kostrov 1974; Tinti *et al.* 2005; Mena *et al.* 2010). We also measure stick-slip stress drop and its evolution with time (Fig. 4b). Note that stress is shown relative to zero at the end of the dynamic slip instability.

Consistent with what is shown in Fig. 1(d), stick-slip behaviour is influenced by LPV, resulting in different shapes of the SVFs (Fig. 4a), peak slip velocities (Fig. 4a) and stress drops (Fig. 4b). Note that at normal stress of 75 MPa this change of attributes is not gradual, but it occurs more rapidly within a certain range of LVPs. In particular, the stick slip events can be grouped according to three LPV ranges. For LPV $\leq$0.5 μm s^{-1}, the events show similar SVF shape (slightly left-asymmetric), duration (∼0.3 s), peak velocity (>100 μm s^{-1}) and stress drop (>1 MPa). Between 0.75 and 1 μm s^{-1}, the peak slip velocities become highly variable (Figs 4a), ranging from 30 to 300 μm s^{-1}, without a recognizable pattern in time or displacement. At LVP of 2 and 3 μm s^{-1}, we find only slow lab-quakes, with peak slip velocities <100 μm s^{-1} (Figs 4a and 5a). This change of stick-slip attributes is more gradual at σ_N = 100 MPa (Figs 4a and 5a), even though the largest transition is again observed between LPVs of 0.75 to 1 μm s^{-1}. The stress drop appears to reduce smoothly with LPV for both values of normal stresses (Fig. 4b). These observations suggest that serpentinite faults are more complex than expectations based on a simple, linear evolution of k_c with LPV (Fig. 2 and eq. 1).

The complexity of slip behaviours and lab-quake characteristics is confirmed by the SVFs. The SVFs for serpentinite faults show systematic changes in shape and symmetry. We note in particular the symmetry of SVFs relative to the peak slip velocity (Fig. 4). At σ_N = 75 MPa, the SVFs tend to be mostly left-asymmetric, that is the peak slip velocity is achieved before half of the entire duration of the event (Figs 4a and S6). This asymmetry, however, tends to decrease with increasing LPV (Figs 4a and S6), when SVFs switch to right-asymmetric. At $\sigma_N = 100$ MPa, the SVFs are mostly symmetric or right-asymmetric (Figs 4a and S6) with the exception at low LPVs (0.1–0.2 μm s^{-1}), which are slightly left-asymmetric. Overall, we observe that symmetric to right-asymmetric events are slower than lab-quakes with left-asymmetric SVFs (Figs 4a and S6c,d). We discuss these features more in detail in the Supplementary section SIII (Fig. S6).

The dependence of the shape of the SVFs on normal stress and LPVs suggests that the shear fabric of the gouge layer plays a role in accommodating the imposed external load and controls the mode of slip and fault's behaviour.

4.2. Interseismic creep

Between each stick-slip event the fault zone is neither fully locked nor stably sliding (Fig. 1). For our range of conditions (Table 1) fault slip (measured by the on-board LVDT) is non-zero during the interseismic phase and begins to accelerate as indicated by the concavity of the displacement-time curves (Supplementary section SIV and Fig. S7). Furthermore, the amount of displacement also increases non-linearly with shear stress (Fig. 5a), indicating non-elastic loading associated with fault creep. This condition is reproducible across consecutive stick-slip events and thus there must be a linear dependency of cumulative slip with the state of stress of the fault (e.g. see selected events at LPV = 0.3 μm s^{-1} and σ_N = 75 MPa, Fig. 5b). Indeed, Fig. 5(b) shows that the local creep velocity is a function of the shear stress according to an exponential law. The proportionality between the logarithm of creep velocity and shear stress is 0.34, which is comparable to values retrieved for dislocation glide in biotite (Kronenberg *et al.* 1990), and considered

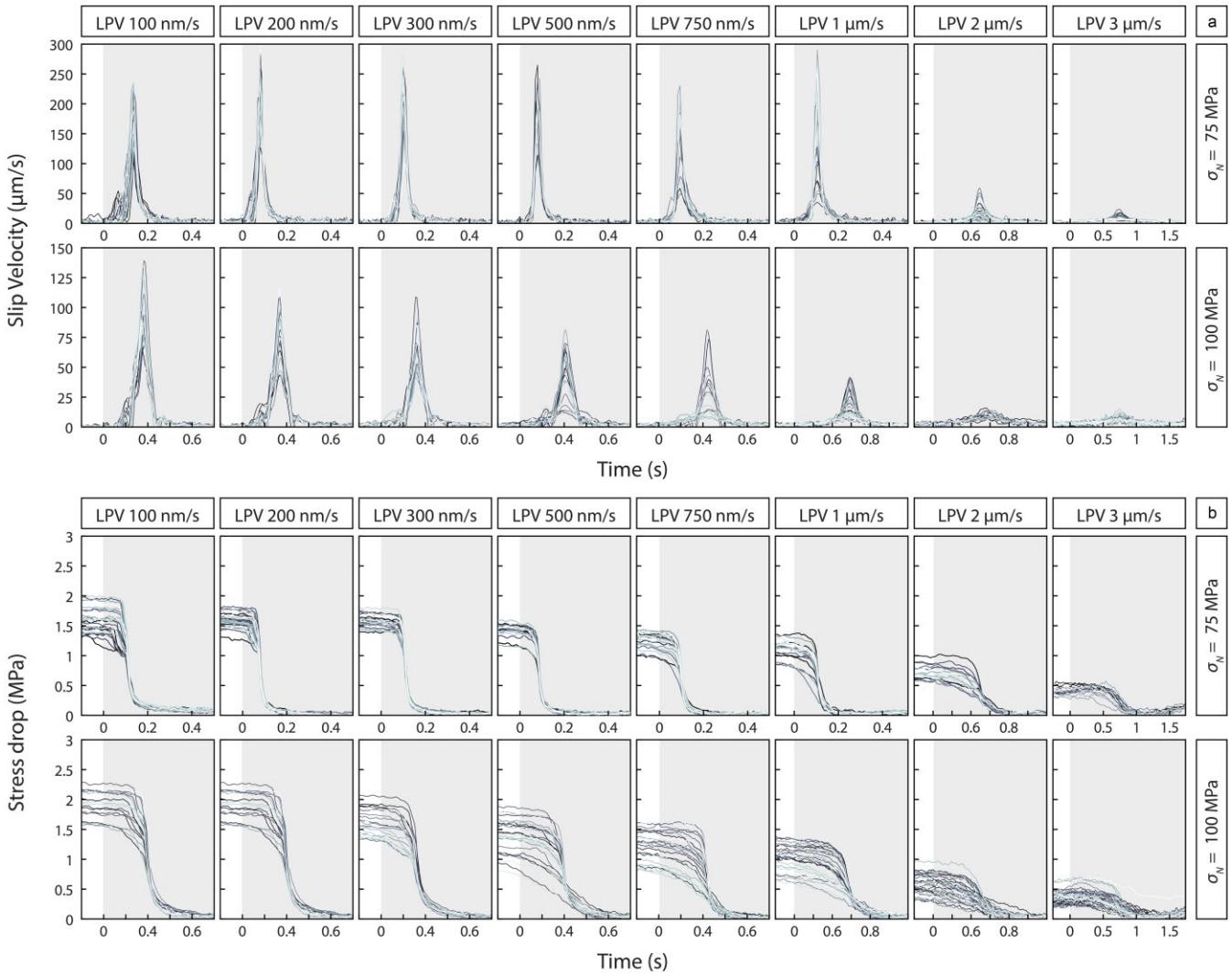

Figure 4 Slip velocity and stress drop time histories:evolution of fault slip velocity (slip velocity function) and shear stress variation in time. The 'stress drop' reported here corresponds to the variation of shear stress during the dynamic event, thus the minimum value is 0. The grey colour scale of the curves, form dark to light, indicate the relative succession in time of the dynamic instabilities. From the slip velocity functions (a) note that, at $\sigma_N = 75$ MPa, the events are similar up to loading point velocities (LPV) up to 500 nm s^{-1}. The slip velocity function becomes variable among subsequent events at LVPs of 750 nm s^{-1} and 1 µm s^{-1}. At higher LVPs, the slip velocity functions have dramatically lower peak velocities. This transition is less pronounced at $\sigma_N = 100$ MPa.

a valid creep mechanism in lizardite (Reinen *et al.* 1992). A power-law fit could also be used, as it graphically overlaps the power-law fit, and yields a large stress exponent $n > 27$ ($R^2 \approx 0.97$). Amiguet *et al.* (2014) also found that lizardite deforms plastically with low strength (differential stress of 20–200 MPa) and that the mechanism is almost insensitive to pressure and temperature.

Although accelerated creep between stick slip events has been documented in many previous studies (e.g. Scholz *et al.* 1972; Anthony & Marone 2005; Scuderi *et al.* 2016; Leeman *et al.* 2018; McLaskey 2019; Cebry *et al.* 2022), the underlying mechanism is often poorly understood. The observation of accelerated creep together with shear stress increase points to plastic flow of serpentinites at low effective loading rates. The good agreement with flow laws previously associated with lizardite (Reinen *et al.* 1992) supports this hypothesis. Nonetheless, the bulk expression of creep in serpentinite faults is likely a complex combination of frictional-plastic mechanisms at the asperity scale, yielding large uncertainties when extrapolating laws for a microphysical model.

4.3. Scaling of the mechanical properties of dynamic events

Our laboratory experiments reproduce a series of stick-slip events following the response of a spring-slider system. The governing equations of a simple spring slider link the mechanical properties of stick slip events with the boundary conditions. Fig. 6(a) shows the scaling of stress drop with peak slip velocity during dynamic slip instabilities. Colours indicate the loading point velocity, transparency the normal stress values. For both investigated normal stresses values the logarithm of stress drop (MPa) scales linearly with the logarithm of peak slip velocity (µm s^{-1}), yielding a power law with exponent ∼0.4 (Fig. 6a). The highest values of both shear stress and peak slip velocity are obtained at LPV values ≤0.5 µm s^{-1} (cold colours in Fig. 6a) and are associated with short acceleration time in SVFs (Fig. S6a). The central values of stress drop and peak slip velocity within this cluster are ∼1.75 MPa of and ∼200 µm s^{-1}, respectively. At higher LPVs (≥0.75 µm s^{-1}), shear stress and peak slip velocity

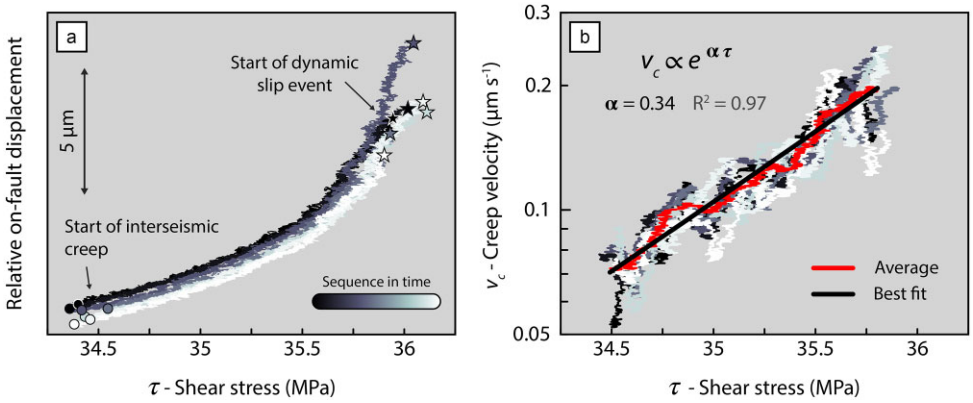

Figure 5 Interseismic creep: interseismic creep paths of seven stick slip events at LPV = 0.3 μm s^{-1} and σ_N = 75 MPa (b1000). (a) Fault slip as a function of shear stress showing the trajectory during stick-slip events. (b) Fault slip velocity as function of shear stress. Best fit (thick black line) using a simplified exponential law links shear stress with creep velocity. Since the effective thickness of the deforming layer is not retrievable from experiments, while assuming it to be constant as a first approximation, the scaling here proposed does not consider the strain rate but the creep velocity. Temperature effects are ignored due to negligible heat production at low slip velocities and low sensitivity to temperature of micas and lizardite (Kronenberg *et al.* 1990; Reinen *et al.* 1994). Curves in panel (a) are shifted rigidly in displacement and slightly overlapped for visualization purposes.

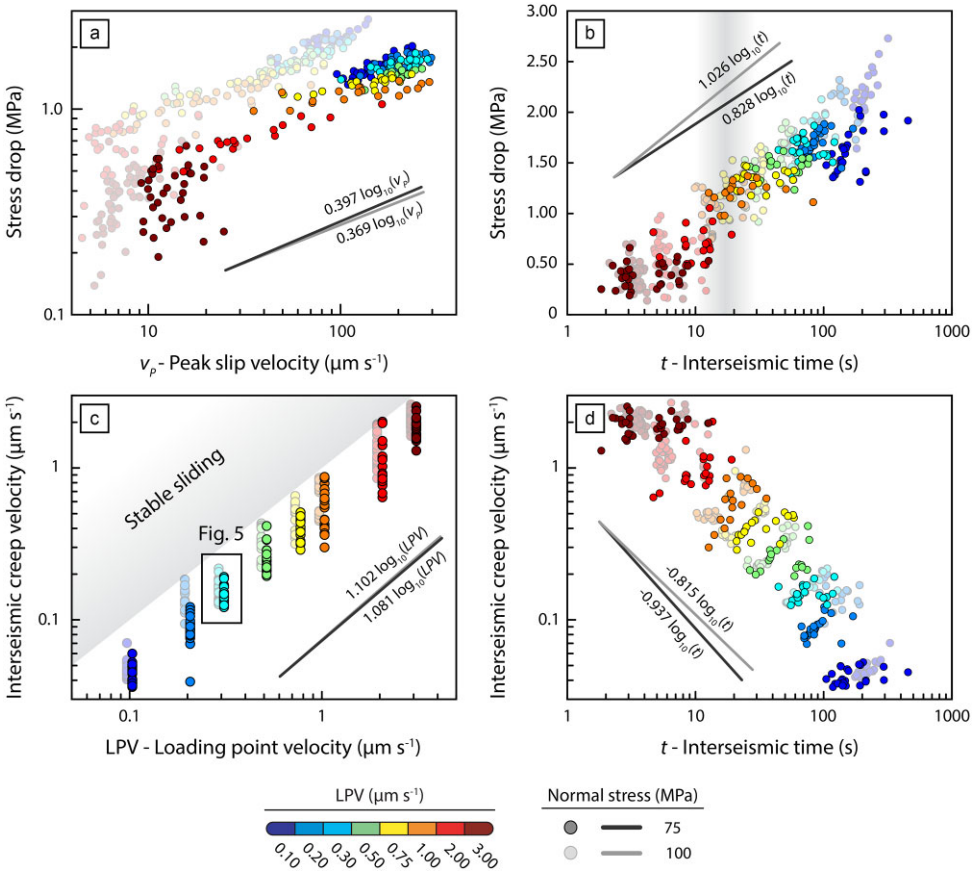

Figure 6 Mechanical properties of stick-slip and scaling relations: (a) stress drop as function of peak slip velocity, dashed lines show the best fit of the linear (in log–log scale) trend; (b) stress drop as function of the time intercurred from the previous event, the shaded area represent the transition in stick-slip behaviour described in paragraph 4.1 (LPV ≈ 1 μm s^{-1}); (c) interseismic creep velocity as function of loading point velocity (points are slightly offset to show better the differences in normal stress) and (d) of time intercurred from the previous event. Transparency indicates the normal stress: opaque for σ_N = 75 MPa and faded for σ_N = 100 MPa. Oblique bars indicate the slope of the best-linear fit of the data (dark and light grey lines for σ_N = 75 and 100 MPa, respectively).

values scale following the inferred linear trend until the transition to stable sliding (LPV = 3 μm s^{-1}), where stress drop values are scattered and peak slip velocities become close to their minimum values approaching the LPV. Stress drops and peak slip velocity values increase at σ_N = 100 MPa following again a linear scaling in log–log space according to a power law with exponent of ∼0.37, and a relatively wide range of peak slip velocities may occur at any given LPV. Deviation from the linear trend and severe scattering

of the data is again observed close to the stability transition at LPV $= 3$ μm s^{-1}.

Stress drops scale linearly with the logarithm of the interseismic time (Fig. 6b), which, for each event, is calculated as the time elapsed since the previous dynamic event. This exponential scaling is similar to the effect of a frictional healing with hold time equal to the interseismic time (e.g. Karner & Marone 2000). The scaling (slopes in Fig. 6b) can be converted to equivalent frictional healing rates of ∼0.01 log^{-1} s, which are comparable with those of granular materials but not matching the ones measured in magnetite–serpentinite gouges in this work. For distinct loading point velocities, we also would expect (eq. 2 of Karner & Marone 2000) a linear relationship between interseismic time and stress drop, which is governed by the loading system stiffness. Apart from low LVPs (alignment of data points at LVP ≤ 0.2 μm s^{-1}, Fig. 6b), this is not observed in our experiments. In fact, the mechanical data scatters around the rough average value of interseismic time and stress drop predicted by purely elastic-frictional theory (Karner & Marone 2000).

In order to get a rough magnitude of the interseismic creep velocity (ICV) we use a simple least squares linear fit of fault displacement to obtain the average slip velocity. The ICV shows a power-law scaling with loading point velocity with larger dispersion with increasing LPV (Fig. 6c). The intersection between the stable sliding threshold (LPV = ICV, Fig. 6c) and the power-law fit occurs at LPVs of minimum 400 μm s^{-1}, far above the suppression of instabilities. This limits the use of the inferred scaling for identifying the transition to stability.

ICV scales also with interseismic time according to a power law, but with negative exponent (Fig. 6d). If each LPV is considered individually, instead, we observe the opposite: a positive scaling between the ICV velocity and the interseismic time. This latter is explained by the fact that, at a given loading rate, the interseismic creep contributes negatively to the storing of elastic energy thus delaying the achievement of peak stress before failure. Interestingly, we find that the investigated normal stresses do not strongly affect the inferred scaling relationships represented in Figs 6(c) and (d). This observation suggests that, at high stresses (75–100 MPa), the first order control on the spring-slider behaviour of this experimental design is exerted by loading point velocity and apparatus stiffness.

Nonetheless, if each single LPV is considered in isolation, we observe an evident scattering of the parameters shown in Fig. 6 around the inferred bulk trends. On one hand, stress drop values show a random scattering in their scaling with peak slip velocities and interseismic time, which is coherent with the observed emergence of different slip velocity functions (see Figs 4 and S6b). On the other, the ICV displays a clear scaling with interseismic time. The largest scattering of data is always observed at high LPV values ($\geq$0.75 μm s^{-1}), where interseismic creep is close to the LPV and the interseismic time is small, suggesting an increased chaoticity of the system. The inferred features characterizing the mechanical properties observed so far call for a detailed investigation of the deformed materials. In the next section, we document that shear fabric evolution can give important insights on the macroscopic frictional properties of the experimental fault.

5 MICROSTRUCTURAL ANALYSIS

Kinematic sections of each of the four experiments used for the characterization of frictional properties were documented with SEM back-scattered imaging. The microstructural investigation was carried out on polished cross-sections using a JEOL JSM 6500F SEM (equipped with a field emission source) using a voltage of 15 keV and a working distance of 10 mm. Figs 7 and 8 show the overall fault textures and close-ups of the most deformed regions.

Magnetite-rich serpentinite samples display an overall Y-B-P-R type fabric (Figs 7a–d) typical of granular-dominated materials (e.g. Logan 1979; Volpe *et al.* 2022b and references therein). Deformation bands are characterized by intense comminution and fabric development and show strong contrast with the low-strain regions that, especially at low normal stresses, are almost undeformed. The principal slip zone (PSZ) is recognizable from the smaller grain size with respect to the surrounding material and the development of a penetrative S-C foliation (Figs 7e–h). The PSZs are present as prominent boundary (B) shear bands.

At low stress, $\sigma_N = 25$ MPa, the bulk of the experimental sample shows little deformation beyond that related to compression during loading. These samples do not have shear fabrics nor significant grain size reduction (Fig. 7a). Only at one side of the sample, at the contact with the central block of the DDS configuration do we observe a shear band that is parallel to the shear motion (Fig. 7e). This few microns-thick PSZ (orange shading Fig. 7a) is formed by extremely comminuted lizardite platelets filling the gaps between much coarser grains (Fig. 7e). The material outside the PSZ is almost undeformed.

At higher stresses, deformation is localized on both boundaries with the forcing block, where shear zones (boundary shear zone) with non-zero thickness are characterized by grain size reduction and fabric development (orange-shaded areas, Figs 7a–d). At the highest normal stress, $\sigma_N = 100$ MPa, some minor shear zones nucleate away from the teeth of the forcing blocks (Fig. 7d). Grain size reduction becomes more widespread and pervasive with increasing normal stress. Grain size reduction is also observed within Riedel shear bands and, at $\sigma_N = 100$ MPa, P-shear bands (R and P, respectively, Figs 7a–d). These features are easily recognizable from splitting along favourably oriented plates of lizardite during decompression.

The boundary shear zone close to the central forcing block is always thicker and with prominent textures. Therefore, we consider them as the principal slip zones that accommodate most of the deformation of each sample. In the main PSZ, we observe a foliated matrix of lizardite enveloping porphyroclasts of dominantly magnetite, diopside and residual clasts of serpentinite. The matrix is extremely fine-grained, with platelets varying from few microns to sub-micron in length, with closely spaced S-C fabric (Figs 7f–h). The spacing between C planes decreases with increasing degree of comminution and roundness of the porphyroclasts fraction at increasing normal stress (compare Figs 7g and h).

The pure lizardite sample displays instead an S-C-C' type fabric (Fig. 8a) that is typical of phyllosilicate-dominated materials (e.g. Bos & Spiers 2001; Volpe *et al.* 2022b and references therein). Deformation is distributed within the entire layer (Fig. 8a) and is characterized by penetrative and closely spaced C' foliation, decorated by S-foliation, traceable to the grain size scale (Fig. 8b). We do not observe continuous nor undulous C foliation as in the case of magnetite-rich serpentinite PSZs (Figs 7f–h), with local exception at the shear boundaries (Fig. 8b). Few porphyroclasts of lizardite and rare clasts of magnetite are dispersed in the phyllosilicate matrix.

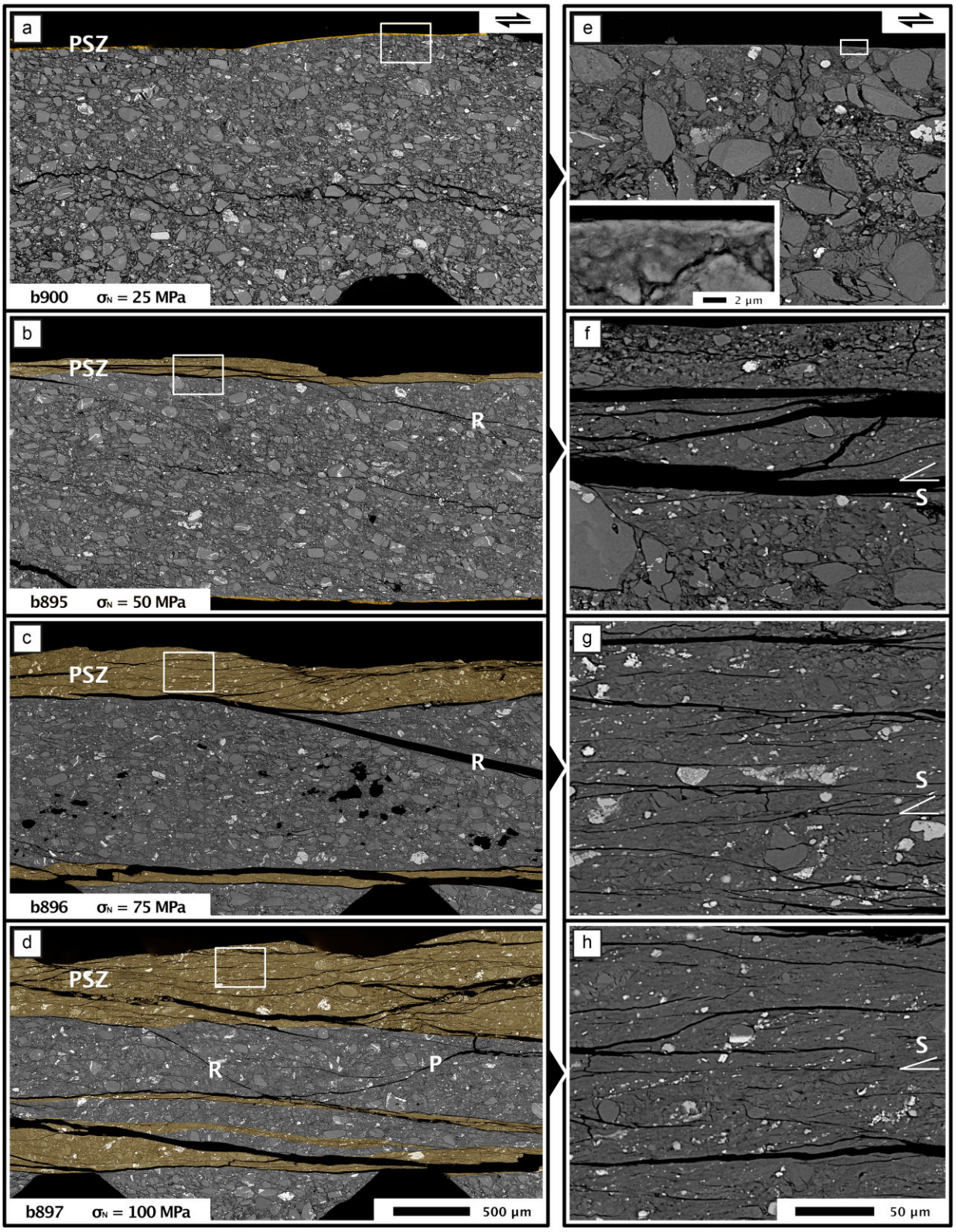

Figure 7 Back-scattered SEM images of Mt-rich serpentinite: Panels (a–d) show the bulk experimental fault architecture, mainly separated in shear bands of high deformation (orange shading), among which is the principal slip zone (PSZ) and almost undeformed low-strain domains. Panels (e–f) show the magnification of the fabric within the PSZs, whose location is highlighted by white frames. The inset in e) shows the close-up of the white frame within. The scale is maintained for each column. All microstructures are oriented to show dextral shear sense. R—Riedel (normal motion) shear bands, P—compressive (inverse motion) shear bands.

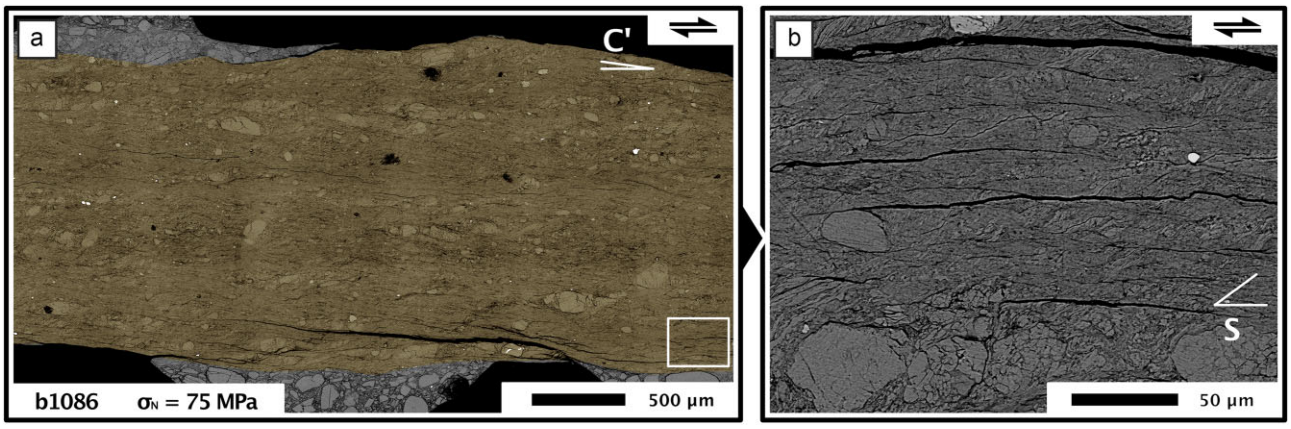

Figure 8 Back-scattered SEM images of lizardite: (a) bulk experimental fault architecture, characterized by distributed deformation (orange shading) and pervasive S–C' foliation. (b) magnification of the foliation within the white frame. All microstructures are oriented to show dextral shear sense. C'–C' foliation, S–S foliation.

6 DISCUSSION

Magnetite–lizardite serpentinite powders display a complex frictional behaviour that depends on the imposed loading point velocity and normal stress conditions. It is well-known that rock fabric influences the rheological and frictional behaviours of experimental faults (e.g. Holdsworth 2004; Niemeijer *et al.* 2010; Scuderi *et al.* 2020; Collettini *et al.* 2021; Bedford *et al.* 2022; Volpe *et al.* 2022a), implying that the integration of microstructural and experimental data is key to understanding the phenomenology of fault friction.

6.1. Nucleation of instabilities due to rate-dependent friction

The first order observation of the mechanical behaviour of magnetite-rich serpentinites is that slip can be accommodated stably or unstably (stick-slip) depending on the applied normal stress and loading point velocity (Figs 1c and d). According to theory, instability occurs when the material is velocity weakening [negative (a–b), Fig. 2b] and if the fault weakening rate with slip, that is the critical stiffness, is higher than the loading system stiffness (eq. 1, e.g. Gu *et al.* 1984; Rice 1983).

We measured the RSF parameters (a–b) and D_c to obtain the normalized critical stiffness (k_c) as a function of the sliding velocity (eq. 5). In our experiments, the k_c of magnetite-rich serpentinite varies as a function of the sliding velocity and rapidly decreases with LPV. (Fig. 2d). This agrees with the emergence of unstable slip at low sliding velocities and the transition to stable sliding at higher slip rates. The second ingredient of eq. (1), the normalized stiffness of the loading system (k), needs to be measured to find the exact velocity range in which unstable sliding is expected.

For our experiments, the effective loading stiffness k includes the elastic parameters of the apparatus and those of the sample. We measure k from the linear part of the friction versus loading point displacement record of stick-slip events (Fig. 9a, greyscale curve and angle). However, we need to account for interseismic creep (Fig. 5, Section 5.2), because they contribute for part of the measured load point displacement. Aseismic fault creep and deformation within the fault zone contribute to dissipate part of the stored elastic energy in the system (Fig. 9c). Thus, the stiffness k estimated using the loading point displacement (Fig. 9a, grey angle) is only an apparent stiffness (k_{app}), which is an underestimate of the true elastic stiffness. This is highlighted also by the direct relationship between interseismic time and interseismic creep in Fig. 6(c): the faster the interseismic creep, the longer will be the time required (at a given LPV) to accumulate enough elastic energy. To obtain the effective normalized stiffness (k_{eff}), the friction data should be evaluated as a function of the effective elastic deformation of the system (our experimental elastic reservoir).

The elastic deformation of the system (comprehensive of material and machine contributes, blue line, Fig. 9b) can be obtained by subtracting the non-recoverable fault displacement (measured with a sensor close to the experimental fault, green line) from the load point displacement (the position of the loading piston, grey line). We then use k_{eff} to plot the friction data (colour-scale curve in Fig. 9a). The evolution of friction with elastic deformation is now linear and shows no relevant hysteresis during cycles of loading-unloading (Fig. 9a). The slope of this curve (blue angle, Fig. 9) is the effective normalized stiffness k_{eff}.

After this correction, we can compare the effective and apparent normalized stiffnesses (Fig. 10a). Stiffness data are plotted as a function of the degree of locking of the experimental fault, which is represented by the experimental interseismic coupling (EIC):

$$\mathrm{EIC} = 1 - \frac{\mathrm{ISC}}{\mathrm{LPV}}, \tag{5}$$

where ICV is the interseismic creep and LPV is the loading point velocity. This quantity is equivalent to the interseismic coupling measured in natural fault segments (e.g. as defined in Kaneko *et al.* 2010). When the experimental interseismic coupling is 1 the fault is locked (ICV = 0), while if it is equal to 0 it is continuously sliding (ICV = LPV). The experimental interseismic coupling is important for understanding the role of fabric during the stick-slip cycle.

For both considered normal stresses, the apparent normalized stiffness (k_{App}) shows wide variability, especially at high LPVs close to the stability transition (~5 µm s^{-1}). The highest K_{App} values (1.6 and 1.2 mm^{-1} at σ_N = 75 and 100 MPa, respectively) are observed at low LPVs (0.1 µm s^{-1}), when the experimental interseismic coupling is high (0.6–0.7). At increasing LPV, k_{App} decreases and becomes more variable (Fig. 10a). The overall experimental interseismic coupling also decreases. After correction, the effective normalized stiffness (k_{eff}) values retain a similar spread as k_{App} but are much higher, with average values of k_{Eff} = 2.4 and 1.9 mm^{-1} (σ_N = 75 and 100 MPa, respectively, Fig. 10a). For each slip event, we can now divide k_{Eff} by the respective k_c (eq. 1), which is obtained with eq. (5) substituting V with the interseismic creep

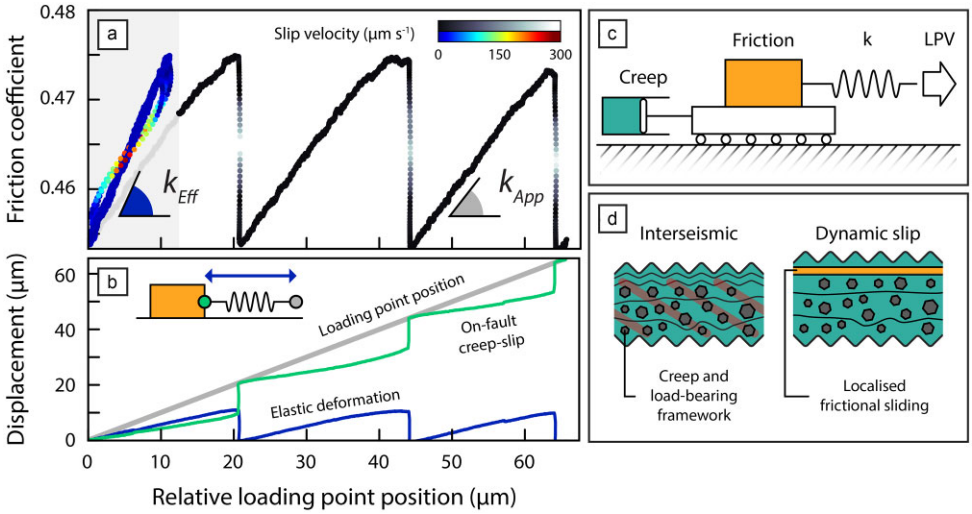

Figure 9 Deformation components and apparent normalized stiffness: (a) friction coefficient for three selected stick-slip events at LPV = 0.1 μm s^{-1} and σ_N = 75 MPa (exp. b1000), expressed as function of the loading point position (greyscale) and the corrected elastic displacement (colour-scale). The colour scale indicates the instantaneous fault slip velocity, the angles indicate the stiffness of the loading apparatus, measured as the slope of the linear fit of the loading path. The grey and blue angles represent the apparent (k_{app}) and effective (k_{eff}) normalized stiffness, respectively. (b) curves of the relative position of the loading point (grey), on-fault creep-slip displacement (green) and the difference between the two (blue line), that represents the elastic deformation used in panel (a). (c) conceptual model of the experimental fault rheology, similar to the CNS model (Chen *et al.* 2017). (d) ideal experimental fault architecture in two phases of the seismic cycle. Green colouring represents the viscous contribute, orange the frictional one.

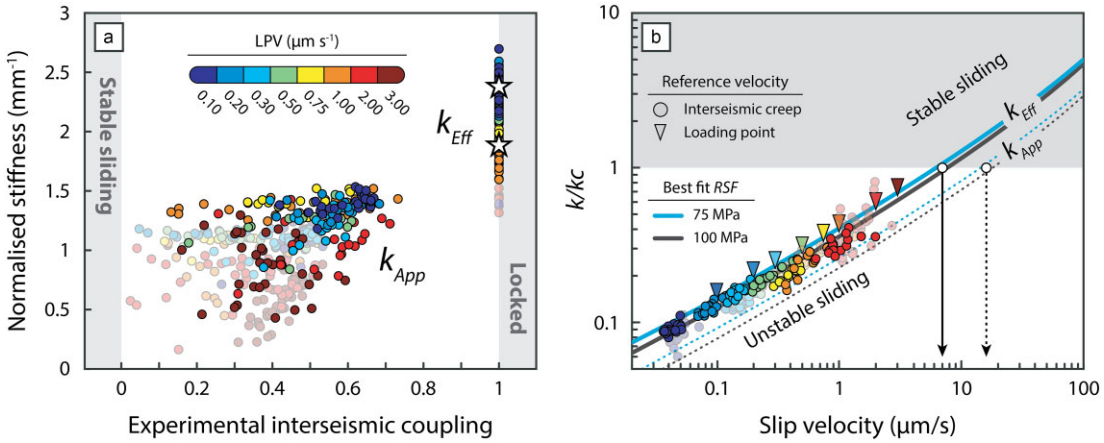

Figure 10 Effective stiffness and fault stability: (a) comparison between apparent (k_{app}) and effective (k_{eff}) normalized system stiffness. The experimental interseismic coupling (EIC) represents the degree of locking of the experimental fault. Since k_{eff} is measured after removing the interseismic creep contribution, values are plotted as if the experimental interseismic coupling is 1. (b) Ratio between the normalized stiffness and the normalized critical stiffness (k_c). Single k_c values are obtained using the interseismic creep velocity values in eq. (5) normalized by the respective k_{eff}. Best-fitting curves are obtained using the average values of k_{app} and k_{eff} (stars in panel a) normalized by the k_c obtained with eq. (5). Values at LPV = 3 μm s^{-1} are not plotted because of difficulties in performing the correction. Arrows indicate the LPV at which transition to stable sliding should occur ($k/k_c = 1$) for both k_{app} (dashed line) and k_{eff} (solid line).

velocity, which is the average on-fault velocity in the interseismic period. The values scale coherently with the theoretical curve of k/k_c (solid lines, Fig. 10b) obtained using the best fit of k_c and the average k_{eff}. The transition to stable sliding ($k/k_c > 1$) is predicted at a LPVs of 8 and 6.5 μm s^{-1} (at σ_N = 75 and 100 MPa, respectively, Fig. 10b, solid line arrow), which are close to the LPVs at which the transition to stable sliding is observed in our experiments (>5 μm s^{-1}). Using k_{App} instead (dashed lines in Fig. 10b) the transition would be predicted at far higher LPVs > 18 μm s^{-1} (Fig. 10b dashed arrow) where the observed sliding is stable.

We have demonstrated that, although the deformation of the experimental fault is controlled by both viscous (creep) and elastic-frictional components, the rate and state framework is efficient in predicting the stability transition when the dependence of its constitutive parameters on sliding velocity is considered. This analysis is feasible only after appropriate separation of the two components.

6.2. Microstructural interpretation of creep-slip behaviour

Frictional instabilities observed in lizardite–magnetite serpentinite are not present in pure lizardite powders under the same experimental boundary conditions (Fig. 1b). This implies that the frictional properties that lead to unstable slip must be related to magnetite, which is the dominant granular phase, in rheological contrast with the serpentine (e.g. Tarling *et al.* 2018). Several previous works have shown that mixed phyllosilicate-granular powders possess similar

dependence of rate and state friction on the sliding velocity (Saffer *et al.* 2003; Ikari *et al.* 2011, 2013; Moore *et al.* 2016; Ruggieri *et al.* 2021; Scuderi *et al.* 2022; Volpe *et al.* 2022a). We suggest that the complex rheology arises due to the interplay of the two mineral components. Here, we integrate mechanical data with microstructural analysis to provide a qualitative model for the origin of creep-slip in phyllosilicate-granular mixtures.

Our results suggest that shear motion forms an S-C-C' fabric in the principal deformation zones of magnetite-rich serpentinite faults. This microstructure, typical of phyllosilicate-rich gouges (e.g. Bos & Spiers 2001; Volpe *et al.* 2022b and references therein), presents through-going, anastomosing C-foliation that curves around the boundaries of porphyroclasts (Figs 7c and d). The interconnectivity of the weak lizardite platelets is highlighted by the formation of this foliation (Figs 7f–h). Even though the c-planes are the most favourably oriented to accommodate shear motion, their undulous character suggests that the porphyroclasts produce local stress inhomogeneity and may form a load bearing framework (Fig. 9d). The load bearing framework is expressed as the stiff interaction of granular materials across the fault, which can form force chains (Fig. 9d). This is evident from comparison of microstructures with those of the experimental faults that did not show frictional instabilities: the one deformed at $\sigma_N = 25$ MPa (Figs 7a and e), and the pure lizardite experiment (Fig. 8a). The first shows extremely localized deformation corresponding to a single layer of lizardite platelets (Fig. 7e), which does not include granular phases. The second shows distributed deformation, low-angle S–C' foliation, typically associated to velocity-strengthening materials that prevent hard interaction of the granular phase (Haines *et al.* 2009, 2013; Okamoto *et al.* 2019; Volpe *et al.* 2022b). The formation of a stiff load-bearing framework is therefore necessary for the build-up of elastic energy which would be otherwise entirely dissipated by the phyllosilicate matrix. Stable slip due to viscous deformation at low sliding velocities is postulated by microphysical models assuming rate-dependent rheology of the frictionally stronger phase (e.g. Reinen *et al.* 1992, 1994; Chen *et al.* 2017; Aharonov & Scholz 2018; Allison *et al.* 2018; Barbot 2019; van den Ende *et al.* 2018).

The presence of a partial load bearing framework is also inferred from the analysis of frictional healing during slide-hold-slide tests (Figs 1a, 3 and 11). Indeed, on closer inspection, the frictional healing values are not distributed linearly but start decreasing systematically only when hold times exceed 10 s (Fig. 3b). This change is associated with a difference in the evolution of friction that follows each hold. We first observe that friction increases rapidly upon reshear to a peak value, immediately followed by a decrease to a minimum value (Fig. 11a). This friction value is smaller than the steady-state friction measured before the hold, and decreases systematically with hold times above 10 s. Following the minimum, friction increases with slip until pre-hold values are attained. With these observations we can separate the frictional healing in two components: a negative and a positive one, as illustrated in Fig. 11(a). The sum of two components yields the bulk frictional healing (Fig. 3b). Both negative and positive components of frictional healing display a distinct linear trend only when hold times are larger than 10 s (Fig. 11b).

We interpret the positive component of healing as a proxy of the formation of the partial load bearing framework while the negative component represents the bulk relaxation (mobility) of the phyllosilicate network. The latter is confirmed by the fact that the creep relaxation rates of both serpentinite and lizardite are similar, and also identical to their respective negative healing rates (Fig. 11c). The absence of granular phases in the pure lizardite yields a bulk negative healing rate (e.g. Tesei *et al.* 2012) and the negligible positive component. The positive healing component in the mt-rich serpentinites may explain the positive scaling between stress drop and interseismic time (Fig. 6b), which would otherwise be puzzling due to the bulk negative healing (Fig. 3b).

The transition from unstable to stable regime can therefore be illustrated as the competition between the purely elasto-frictional deformation of the granular fraction (see previous section) and the viscous-frictional deformation of the phyllosilicate matrix. At low loading rates, the lizardite matrix responds viscously (Reinen *et al.* 1992, 1994; Amiguet *et al.* 2014) around magnetite porphyroclasts, allowing for the recovery of a granular load bearing framework. This is confirmed also by the creep relaxation that, if measured in shear stress, is independent from the normal stress (compare Fig. 11d with Fig. 3d). Upon re-shear, dilation lowers dramatically the interaction of the granular fraction (e.g. Chen *et al.* 2017) while promoting frictional sliding on the lizardite platelets. The phyllosilicate matrix, incapable to flow around porphyroclasts in this regime, behaves similarly to pure lizardite gouges with macroscopic stable sliding. It should be noted that, even at the lowest loading rates, the experimental interseismic coupling of lizardite–magnetite serpentinite is smaller than 1 (Fig. 10a), implying that the load bearing framework is only partial, and the locking of the fault is function of the mobility of the phyllosilicate matrix. This gives rise to a creep-slip—rather than stick-slip behaviour—very similar to those predicted by numerical simulations of visco-frictional rheologies (Allison *et al.* 2018). The integration of viscous rheology with rate and state friction can be instrumental to encompass the complex spectrum of fault slip behaviour in complex materials (e.g. Pranger *et al.* 2022).

6.3. The timescale of deformation processes

We have observed that rate- and state-dependent friction theory, associated with velocity-dependent constitutive parameters, explains the first order behaviour of the experimental fault. However, the purely frictional framework is not sufficient to predict the variability of the mechanical properties of stick-slip events (see Sections 5.1 and 5.3). Foremostly, complex stick-slip events should emerge close to the bifurcation expressed by eq. (1) according to theory (Gu *et al.* 1984). Moreover, if k_c decreases with velocity (e.g. Baumberger 1994; Leeman *et al.* 2016, 2018), the slip events can be slow when the (k/k_c) ratio is close to 1 ($k/k_c > 0.7$, Leeman *et al.* 2018). In our experiments, all of the lab-quakes (Fig. 4) are categorizable as 'slow' even though the associated (k/k_c) ratios can be as small as 0.1 (Fig. 10b). We also observe different slip velocity functions at the same (k/k_c) ratio and loading rate but different normal stress values (Figs 4a and S6a). Although the shape of the slip velocity function can be the result of the variation of rate and state parameters with slip velocity (e.g. Im *et al.* 2020), the equation that describes this dependency in our experiments (eq. 5) is not substantially affected by the normal stress (Fig. 10b). These observations suggest that unstable slip in magnetite-rich serpentinites is the result of multiple deformation mechanisms that, together, define the macroscopic behaviour of the experimental fault.

The binary nature of the gouge, phyllosilicate-granular, is reflected by the coexistence of viscous-frictional and elastic-frictional mechanisms. Both mineral components control the bulk frictional response but operate at different time scales or, in other words, they respond more or less steadily to the change of external (e.g. velocity stepping, and slide hold slide tests) and local forcing. The fastest

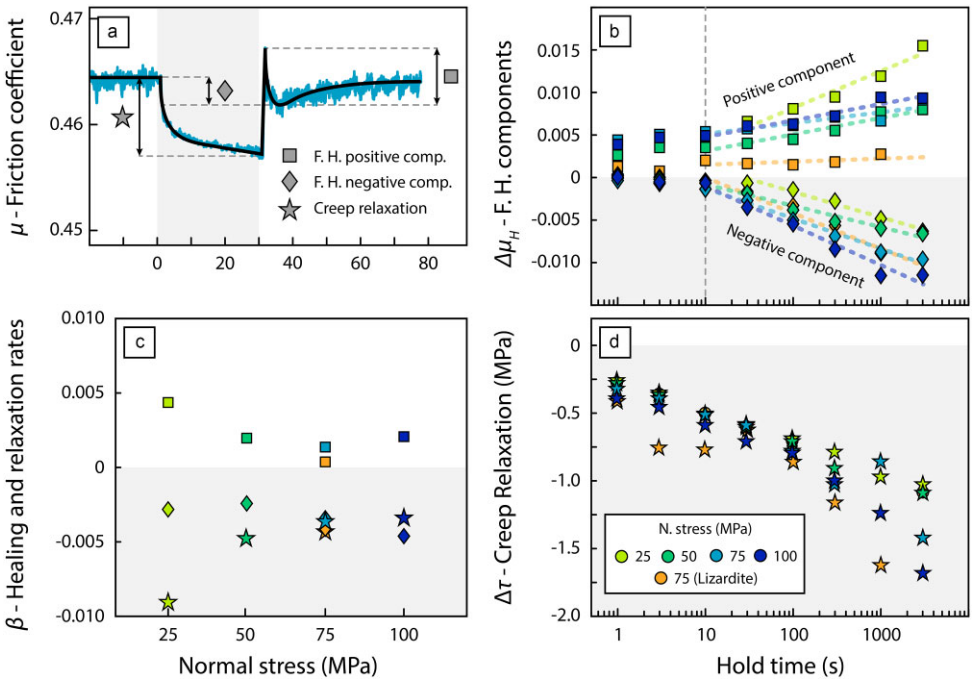

Figure 11 Frictional healing components and creep relaxation: (a) the same example of slide-hold-slide test of Fig. 3(a), where frictional healing ($\Delta\mu_H$) is separated in its positive (squares) and negative (diamonds) components, creep relaxation is again reported with the star symbol; (b) values of positive and negative components of frictional healing measured at increasing hold times, with dashed lines representing the linear fit (lin–log space) whose slope, the healing and relaxation rates (β), are reported in panel (c) and (d) creep relaxation expressed in stress drop instead of friction (compare with Fig. 3d) as function of logarithm of time.

response is that of the granular framework, dominated by magnetite grains. This material deforms according to elastic-frictional interaction of particles due to the equant aspect of grains, the high stiffness, the sluggish diffusion kinetics and the high friction angle (Österle *et al.* 2014). The timescale of this process is likely very small, possibly proportional to D_c and the state variable (eq. 3). The slow, viscous-frictional part is instead controlled by the phyllosilicate network that envelops the granular materials. Its dynamics is the result of plastic deformation by pure glide along the phyllosilicate folia at low forcing stressing rates. The work of Reinen *et al.* (1992, 1994), however, defines a transitional sliding velocity (imposed at the boundary of the experimental shear zone) between 0.32 and 1.0 μm s^{-1}, across which lizardite is observed to have a purely frictional rheology. With this information we can build a microstructural interpretation of the three creep-slip regimes explored in Section 4.1 and the transition to stable sliding.

The key component to obtain frictional instability is the formation of a partial load-bearing framework (Fig. 9d), when the fault is, even partially, locked (experimental interseismic coupling >0 (Fig. 10a), not observed in pure lizardite). Sudden acceleration to dynamic slip may happen every time a zone of stress concentration (jamming of the granular fraction) fails. That is, we suggest a similar initiation mechanism based on force chains in pure granular material (e.g. Mair *et al.* 2002; Pozzi & Scuderi 2022). Unstable slip propagation and stress transfer is then accommodated depending on the rearrangement of the viscous-frictional phyllosilicate matrix, which determines the slowness of the process (slow creep-slip). Finally, the slowness of the viscous deformation of the phyllosilicate matrix is crucial for the recovery of the load bearing framework (frictional healing) during the interseismic phase.

We distinguish three regimes depending on the length of the interseismic time. If the interseismic phase duration (white intervals of Fig. 12) is >10 s, the interseismic creep velocity (blue curve) seats well below the transition velocity (Fig. 12c, cyan line) and a partial load bearing framework can form, resulting in the increase of the apparent and effective *k*, as well as the experimental interseismic coupling (Fig. 10a). The beginning of the unstable slip (on-fault slip rate equal to the LPV) occurs at velocities lower than the transition velocity (Fig. 12c) and dynamic slip builds up with rapid acceleration (left-asymmetric slip velocity functions, Fig. S6). This rapid acceleration is likely the result of local failure of force chains and subsequent deformation of a relaxed phyllosilicate matrix (high negative healing component, Fig. 3d), also aided by weakening caused by sudden dilation (Fig. 12 b). This regime is observed for LPVs < 1 μm s^{-1} (Fig. 5b).

If the interseismic period is lower than 10 s, the interseismic creep velocity remains close to the transition velocity (Fig. 12k) and does not allow the formation of the partial load bearing framework (low k, Fig. 10a). This generates small frictional instabilities characterized by small peak velocities (Fig. 5a), preceded by gradual acceleration (Fig. 12k) and symmetric to right-asymmetric slip velocity functions (Figs 4 and S6). The creep-slip behaviour is accompanied by small dilatancy (Fig. 12j) which indicates reduced interaction of the granular fraction. Lastly, when the average interseismic period is close to 10 s the LPV is comparable to the transition velocity (Fig. 12g). Here, we observe chaotic behaviour with non-predictable alternance of relatively slow and fast events (Figs 5a and 12g), where fast events are characterized by large dilatancy compared to slow ones (Fig. 12f).

The significative timescale of 10 s does not appear to emerge casually. This is in fact the minimum time at which the positive and negative frictional healing components can be confidently measured and distinguished in the slide-hold-slide tests (Fig. 10b). Stick slip events that have an interseismic period longer than 10 s show also

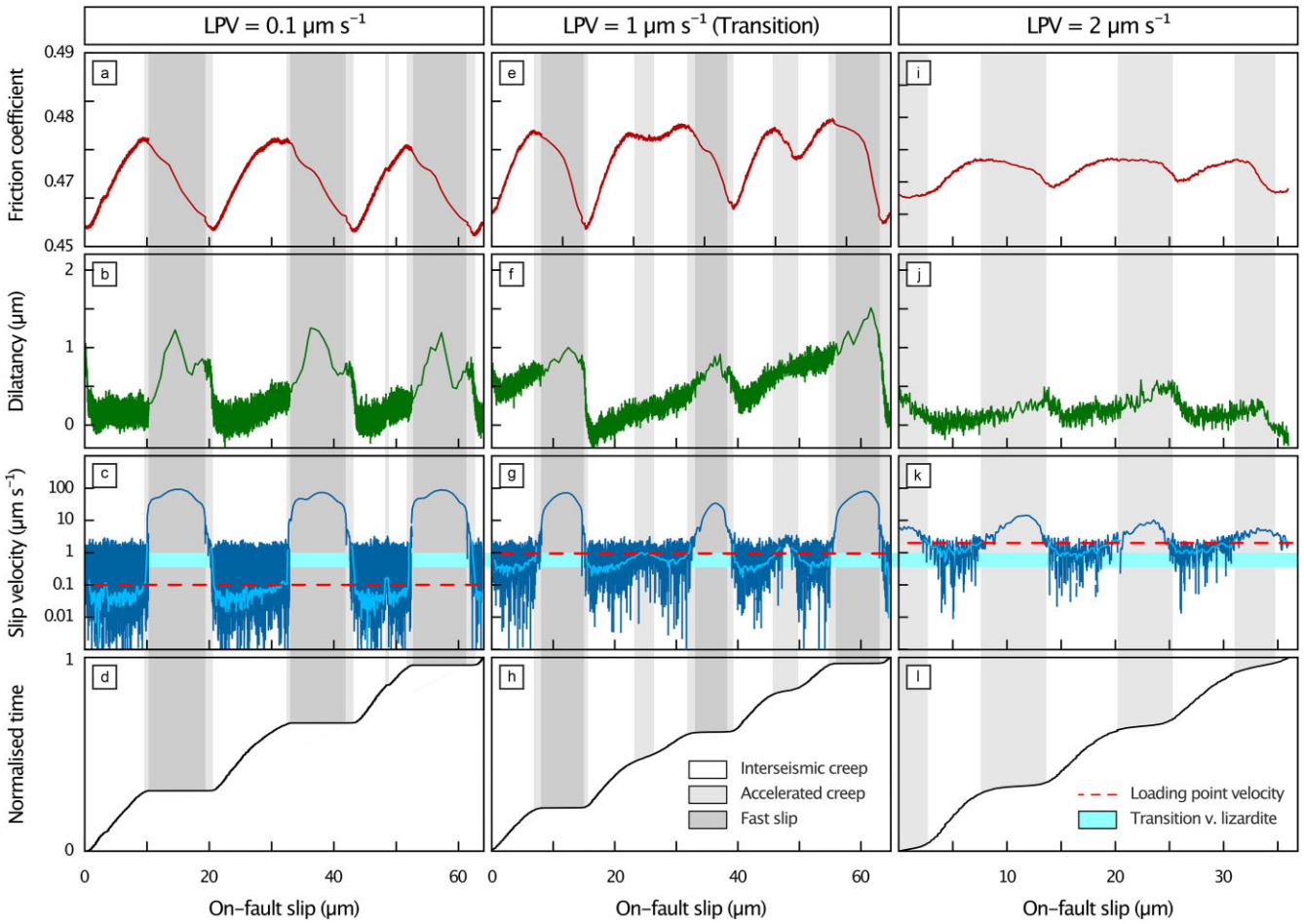

Figure 12 Mechanical comparison of dynamic events: mechanical properties of selected portions of the experiment b1120 ($\sigma_N = 100$ MPa) at LPVs of interest. Red curves: friction coefficient; green curves: recoverable dilatancy; blue curves: slip velocity, treated with low-pass filter and overlaid in lighter blue to better show the low velocities; black: time normalized by the total duration of the selected data. Relatively fast, regular stick slip occurs at LPV = 0.1 (panels a and d). Events become highly variable at LPV = 1 μm s^{-1} (panels eh). Small instabilities with slip velocity comparable to LPV are observed at LPV = 2 μm s^{-1} (panels i–l). Recoverable dilatancy is obtained by removing the bulk trend of shear thinning, which is detrended as the long-term variation of the total layer thickness with on-fault slip. The range of transition velocity of lizardite (Reinen *et al.* 1994) is shaded in cyan.

the higher experimental interseismic coupling, suggesting that these timescales are optimal for the formation of the unstable partial load bearing framework.

Considering two rheological regimes with two different timescales adds a layer of complexity to the first order phenomenology described by the rate and state friction framework. However, this is still not sufficient to explain why there is a substantial difference in slip velocity functions between experiments performed at $\sigma_N = 75$ and 100 MPa. It is also not sufficient to explain why there is such variability of interseismic time (at the same LPV) without any clear link with the mechanical properties measured for each event (Fig. 5 and Section 5.3).

6.4. Heterogeneous fabric, heterogeneous instabilities

The mechanical properties of stick-slip events show a rough, but consistent scaling of stress drop, peak slip velocity, interseismic creep velocity and interseismic time (Fig. 6). Scaling is consistent with the similarity of the sample-machine assembly to a simple spring slider. Deviations are likely a function of the stress history during the succession of unstable events (e.g. Beeler *et al.* 2014; Passelegue *et al.* 2020) but also of the fault fabric; that is, the arrangement—function of time and space—of the granular materials within the phyllosilicate matrix.

The direct and detailed inspection of fabric during deformation is not yet possible, but some micromechanical interpretation can be inferred from the main proxy of the packing state of the granular framework, which is dilation (Figs 12b, f and j). We observe dilation during (i) the interseismic phase (reorientation of partial force chains during nucleation), (ii) the dynamic slip and (iii) the velocity steps (dilation controlled by strain rate, e.g. Chen *et al.* 2017). The cyclicity of dilation-compaction stages is gradually lost towards stable sliding conditions (Figs 12b, f and j), which means that a dilated, steady-state PSZ accommodates deformation with a stable fabric, dominated by the lizardite foliation as in the case of pure lizardite gouges (Fig. 1c). Dilation prevents interaction and jamming of the granular phase, which is microstructurally the most heterogeneous in terms of grain size and spatial distribution (Figs 7e–h).

It is reasonable to assume that more heterogeneous fault fabrics produce greater deviation from a classic spring-slider model. Obviously, this will remain a speculation since we cannot fully express the underlying physics (e.g. Beeler *et al.* 2014) nor exert an absolute control of the external forcing parameters (the experimental apparatus, Gualandi *et al.* 2023). However, there is a macroscopic

effect that can be linked to fault heterogeneity, which is the shape of the slip velocity functions (Section 4.1). At $\sigma_N = 75$ MPa and low loading point velocities, the slip velocity function is left-asymmetric (Fig. 4a), meaning that the instability starts via rapid acceleration and then decays more gradually (Fig. S6a). Our view is that the sudden acceleration initiates via unjamming of the partial load bearing framework, revealed by the relatively high interseismic coupling (Section 7.3 and Fig. 9a). At $\sigma_N = 100$ MPa and the same loading point velocity, the slip velocity function is Gaussian to slightly right-symmetric, that is characterized by a rather symmetric gradual acceleration profile centred on the achievement of the peak slip velocity (Figs 4a and S6a). These differences are reflected by the microstructures since at the highest normal stress deformation is more distributed (compare Figs 7c and d) and the grain size of the granular phase tends to be smaller (compare Figs 7g and h). We have already observed that pure lizardite shows distributed deformation, meaning that the granular phase favours processes of slip localization (Volpe *et al.* 2022b, and references therein). Therefore, at higher stresses, the phyllosilicate network is more efficient in accommodating permanent deformation during the interseismic stages and during nucleation, promoting more gradual acceleration into the dynamic event. This hypothesis is also confirmed by the lower interseismic coupling measured at $\sigma_N = 100$ MPa (even at low LPVs, Fig. 10a) determined by the slightly faster interseismic creep velocity (Fig. 5c). Support comes also from previous study suggesting that the difference in slip velocity functions is determined by fabric heterogeneity (Scuderi *et al.* 2020; Pozzi & Scuderi 2022).

7 IMPLICATIONS FOR NATURAL FAULTS

Serpentinites are significant for the rheology of several tectonic environments (Guillot *et al.* 2015, for a review). They are found in major shear zones at the interface of subducting plates, spreading ridges and orogenic nappe stacks. These bodies localize and facilitate deformation due to their rheological weakness (Hirth & Guillot 2013; Tesei *et al.* 2018), which is the result of a low shear resistance of minerals such as lizardite ($\mu < 0.3$, Reinen *et al.* 1994; Moore *et al.* 1996, 1997; Escartin *et al.* 1997; Moore & Rymer 2007; Tesei *et al.* 2018), which favour deformation along the [001] plane by frictional sliding (eased by bulk development of c-foliation) and dislocation glide. Serpentinites are also sensitive to pressure solution in hydrothermal environments, mechanism that contributes to their bulk weakness (Tesei *et al.* 2018). Due to oriented growth in cracks during shear deformation, only 15 per cent of serpentinization of peridotite is sufficient to decrease the resistance of these rocks to that of pure serpentinite (Escartin *et al.* 2001; Tesei *et al.* 2018; Viti *et al.* 2018). Slip along these weak layers, associated with the velocity-strengthening behaviour recorded in analogue fault material, is argued to favour aseismic creep and to hinder fault instability (Reinen *et al.* 1994; Hirth & Guillot 2013).

Equally numerous experimental studies focus on the relevance of weak fault materials, plenty of field evidence demonstrate that faults are complex objects, where the coexistence of the full range of slip behaviour may occur by deformation partitioned between two rheologically different materials (Fagereng & Sibson 2010; Tembe *et al.* 2010; Collettini *et al.* 2011; Tesei *et al.* 2014; Fagereng & Beall 2021; Volpe *et al.* 2022a). Seismic failure within or along strong lenses (or phacoids) can also be promoted by high fluid pressure due to break-down of hydrated phases (among which serpentinites) during subduction (e.g. Fagereng *et al.* 2014; Behr *et al.* 2018; Tarling *et al.* 2019). Serpentinite shear zones, such as those sampled for this study (Monte Fico, Elba Island, Italy, e.g. Keller & Pialli 1990; Tesei *et al.* 2018), typically display this anatomy of anastomosing levels of weak phyllosilicates that envelop strong, magnetite rich slow-strain domains. In light of this knowledge, our study finds relevance for the rheology of the low-strain domains, considered as potential sites of unstable slip nucleation.

Previously, unstable slip in serpentinites has been linked to phase transition at depth to the rheologically stronger polymorph antigorite (Dengo & Logan 1981; Xing *et al.* 2019), general higher frictional strength of serpentine minerals at high temperatures (>200 °C, Moore *et al.* 1997) and rate weakening behaviour at displacement rates higher than those of plate rate motion (Reinen *et al.* 1994; Moore & Rymer 2007). Our experiments show that serpentinites enriched in granular phases (magnetite and pyroxene), are far more frictionally unstable than pure phases and thus represent the best candidates to nucleate unstable slip. In fact, the measured (a–b) and D_c parameters decrease with decreasing slip velocities (slow strain rates in nature) yielding k_c values that largely exceed the stiffness of the surrounding medium (consider the high stiffness of the loading system measured in our experiments, Fig. 10a). Low strain rates in the strong lenses are typical due to strain partitioning with the weak matrix, as also shown by recent numerical models (e.g. Beall *et al.* 2019). The partitioning is function of the relative abundance of weak phases, contrast of viscosity and external loading rates. We thus infer that, similarly to other tectonic environments (Fagereng & Sibson 2010; Collettini *et al.* 2011; Hayman & Lavier 2014; Beall *et al.* 2019; Fagereng & Beall 2021; Volpe *et al.* 2022a), serpentinites are susceptible of nucleating the entire spectrum of fault slip behaviour (see also French & Zhu 2017; Tarling *et al.* 2018, 2019). The combined effect of nucleation within the strong lenses and propagation within rate-strengthening serpentine materials will determine whether slip will occur stably, with accelerated creep, or with slow-to-fast dynamic slip.

8 CONCLUSIONS

We analysed the frictional behaviour of natural magnetite-rich lizardite gouges as representative rocks of low-strain domains in serpentinite shear zones, acting as potential sites of nucleation of unstable slip.

Lizardite–magnetite synthetic fault gouges display more pronounced velocity weakening behaviour than pure lizardite, indicating low strain domains in natural serpentinite shear zones as preferred sites of nucleation for unstable slip. Thanks to the small critical slip distance (D_c), the force imbalance is met even when the stiffness of the loading medium is high (>180 MPa mm^{-1}) and external loading velocities are much higher than natural plate motion rates (<5 μm s^{-1}). The inverse dependence of the critical stiffness to sliding velocity concur in promoting fault instability, especially at low loading point velocities. Overall, the bulk slip behaviour of serpentinite-hosted experimental faults is accurately described by the velocity-dependence of rate- and state-dependent friction law.

The velocity dependence of rate and state parameters is phenomenologically explained by the distribution of granular and phyllosilicate material in the experimental fault. Slow forcing velocity promotes creep in the phyllosilicate fraction, allowing for creep relaxation at stress concentration sites and promoting a higher degree of packing of the granular fraction. The higher the packing, the

higher is the velocity weakening effect due to enhanced interaction of the granular fraction. With rising slip velocity, dilation and transition to purely frictional regime promotes localization of slip along the weak lizardite foliation with transition towards velocity-strengthening and stable slip conditions.

Not only the mineralogy, but also the fault rock fabric controls the interseismic phase, the nucleation of stick-slip events and the mode in which dynamic slip occurs. Localized deformation and coarser grain sizes promote higher experimental interseismic coupling, fast acceleration at nucleation and left-asymmetric slip velocity functions. Distributed deformation, strong foliation and smaller grain sizes produce gentle acceleration and Gaussian slip velocity functions. Finally, our experiments highlight the role of fault rock complexity in giving rise to unpredictable behaviours of dynamic slip in nature as well as in controlling the slip mode during dynamic instabilities.

SUPPORTING INFORMATION

Supplementary data are available at *GJI* online.

Please note: Oxford University Press is not responsible for the content or functionality of any supporting materials supplied by the authors. Any queries (other than missing material) should be directed to the corresponding author for the paper.

ACKNOWLEDGMENTS

We are grateful to the editor Eiichi Fukuyama, and the reviewers John Bedford and Keishi Okazaki, whose insightful comments improved this paper. We thank Elena Spagnuolo, Giuseppe Volpe, Nico Bigaroni and in particular Elisa Tinti and Cecilia Viti for fruitful discussions and support with the characterization of the sampled materials. We also thank Domenico Mannetta and Manuela Nazzari for their help with microanalytical techniques and sample preparation. Funding of GP and this work is provided from the European Research Council (ERC) project FEAR (grant 856559) under the European Community's Horizon 2020 Framework Programme.

DATA AVAILABILITY

Raw data files are available at https://zenodo.org/record/7938076

AUTHOR CONTRIBUTION

GP: Conceptualization, methodology, investigation, formal analysis, data curation, writing—original draft; CC: Conceptualization, methodology, writing—review and editing; MMS: Conceptualization, methodology, formal analysis, writing—review and editing; TT: Methodology, writing—review and editing; CM: Formal analysis, writing—review and editing; AA: Investigation, data curation, writing—original draft and MC: Data curation, writing—original draft, funding acquisition.

REFERENCES

Aharonov, E. & Scholz, C. H. 2018. A physics-based rock friction constitutive law: steady state friction, *J. geophys. Res.,* **123**(2), 1591–1614.

Allison, K. L. & Dunham, E. M. 2018. Earthquake cycle simulations with rate-and-state friction and power-law viscoelasticity, *Tectonophysics,* **733,** 232–256.

Amiguet, E., Van De Moortèle, B., Cordier, P., Hilairet, N. & Reynard, B. 2014. Deformation mechanisms and rheology of serpentines in experiments and in nature, *J. geophys. Res.,* **119**(6), 4640–4655.

Anthony, J. L. & Marone, C. 2005. Influence of particle characteristics on granular friction, *J. geophys. Res.,* **110**(8), 1–14.

Barbot, S. 2019. Modulation of fault strength during the seismic cycle by grain-size evolution around contact junctions, *Tectonophysics,* **765,** 129–145.

Baumberger, T., Heslot, F. & Perrin, B. 1994. Crossover from creep to inertial motion in friction dynamics, *Nature,* **367**(6463), 544–546.

Beall, A., Fagereng, Å. & Ellis, S. 2019. Strength of strained two-phase mixtures: application to rapid creep and stress amplification in subduction Zone Mélange, *Geophys. Res. Lett.,* **46**(1), 169–178.

Bedford, J. D., Faulkner, D. R. & Lapusta, N. 2022. Fault rock heterogeneity can produce fault weakness and reduce fault stability, *Nat. Commun.,* **13**(1), 1–7.

Beeler, N. M., Tullis, T., Junger, J., Kilgore, B. & Goldsby, D. 2014. Laboratory constraints on models of earthquake recurrence, *J. geophys. Res.,* **119**(12), 8770–8791.

Behnsen, J. & Faulkner, D. R. 2012. The effect of mineralogy and effective normal stress on frictional strength of sheet silicates. *J. Struct. Geol.,* **42,** 49–61.

Behr, W. M., Kotowski, A. J. & Ashley, K. T. 2018. Dehydration-induced rheological heterogeneity and the deep tremor source in warm subduction zones, *Geology,* **46**(5), 475–478.

Blanpied, M. L., Marone, C. J., Lockner, D. A., Byerlee, J. D. & King, D. P. 1998. Quantitative measure of the variation in fault rheology due to fluid-rock interactions, *J. geophys. Res.,* **103**(5), 9691–9712.

Bos, B. & Spiers, C.J., 2001. Experimental investigation into the microstructural and mechanical evolution of phyllosilicate-bearing fault rock under conditions favouring pressure solution, *J. Struct. Geol.,* **23**(8), 1187–1202

Byerlee, J. 1978. Friction of rocks, *Pure appl. Geophys.,* **116**(4–5), 615–626.

Carpenter, B. M., Ikari, M. J. & Marone, C. 2016. Laboratory observations of time-dependent frictional strengthening and stress relaxation in natural and synthetic fault gouges, *J. geophys. Res.,* **121**(2), 1183–1201.

Carpenter, B. M., Marone, C. & Saffer, D. M. 2011. Weakness of the San Andreas Fault revealed by samples from the active fault zone, *Nat. Geosci.,* **4**(4), 251–254.

Cebry, S. B. L., Ke, C. Y., Shreedharan, S., Marone, C., Kammer, D. S. & McLaskey, G. C. 2022. Creep fronts and complexity in laboratory earthquake sequences illuminate delayed earthquake triggering, *Nat. Commun.,* **13**(1), 1–9.

Chen, J., Niemeijer, A. R. & Spiers, C. J. 2017. Microphysically derived expressions for rate-and-state friction parameters, a, b, and Dc, *J. geophys. Res.,* **122**(12), 9627–9657.

Collettini, C. *et al.* 2014. A novel and versatile apparatus for brittle rock deformation, *Int. J. Rock Mech. Min. Sci.,* **66,** 114–123.

Collettini, C., Niemeijer, A., Viti, C. & Marone, C. 2009. Fault zone fabric and fault weakness, *Nature,* **462**(7275), 907–910.

Collettini, C., Niemeijer, A., Viti, C., Smith, S. A. F. & Marone, C. 2011. Fault structure, frictional properties and mixed-mode fault slip behavior, *Earth planet. Sci. Lett.,* **311**(3–4), 316–327.

Collettini, C., Tesei, T., Trippetta, F., Scuderi, M. M., Richardson, E., Marone, C., Pozzi, G. & Viti, C. 2021. The role of fabric in frictional properties of phyllosilicate-rich tectonic faults, *J. Visual. Exp.,* **177,** e62821, doi:10.3791/62821.

den Hartog, S. A. M. & Spiers, C. J. 2013. Tectonophysics influence of subduction zone conditions and gouge composition on frictional slip stability of megathrust faults, *Tectonophysics,* **600,** 75–90.

Dengo, C. A. & Logan, J. M. 1981. Implications of the mechanical and frictional behavior of serpentinite to seismogenic faulting, *J. geophys. Res.,* **86**(B11), 10 771–10 782.

Dieterich, J. H. 1979. Modeling of rock friction: 1. Experimental results and constitutive equations, *J. geophys. Res.,* **84**(B5), 2161–2168.

Escartín, J., Hirth, G. & Evans, B. 1997. Nondilatant brittle deformation of serpentinites: implications for Mohr-Coulomb theory and the strength of faults, *J. geophys. Res.,* **102**(B2), 2897–2913.

Escartín, J., Hirth, G. & Evans, B. 2001. Strength of slightly serpentinized peridotites: implications for the tectonics of oceanic lithosphere, *Geology,* **29**(11), 1023–1026.

Fagereng, Å. & Beall, A.. 2021. Is complex fault zone behaviour a reflection of rheological heterogeneity? *Phil. Trans. R. Soc., A,* **379**(2193), doi:10.1098/rsta.2019.0421.

Fagereng, Å., Hillary, G. W. B. & Diener, J. F. A. 2014. Brittle-viscous deformation, slow slip, and tremor, *Geophys. Res. Lett.,* **41**(12), 4159–4167.

Fagereng, Å. & Sibson, R. H. 2010. Mélange rheology and seismic style, *Geology,* **38**(8), 751–754.

French, M. E. & Zhu, W. 2017. Slow fault propagation in serpentinite under conditions of high pore fluid pressure, *Earth planet. Sci. Lett.,* **473,** 131–140.

Giorgetti, C., Carpenter, B. M. & Collettini, C. 2015. Frictional behavior of talc-calcite mixtures, *J. geophys. Res.,* **120**(9), 6614–6633.

Gu, J.-C., Rice, J. R., Ruina, A. L. & Tse, S. T. 1984. Slip motion and stability of a single degree of freedom elastic system with rate and state dependent friction, *J. Mech. Phys. Solids,* **32**(3), 167–196.

Gualandi, A., Faranda, D., Marone, C., Cocco, M. & Mengaldo, G. 2023. Deterministic and stochastic chaos characterize laboratory earthquakes, *Earth planet. Sci. Lett.,* **604,** doi:10.1016/j.epsl.2023.117995.

Guillot, S., Schwartz, S., Reynard, B., Agard, P. & Prigent, C. 2015. Tectonic significance of serpentinites, *Tectonophysics,* **646,** 1–19.

Haines, S. H., Kaproth, B., Marone, C., Saffer, D. & Van der Pluijm, B. 2013. Shear zones in clay-rich fault gouge: a laboratory study of fabric development and evolution, *J. Struct. Geol.,* **51,** 206–225.

Haines, S. H., van der Pluijm, B. A., Ikari, M. J., Saffer, D. M. & Marone, C. 2009. Clay fabric intensity in natural and artificial fault gouges: implications for brittle fault zone processes and sedimentary basin clay fabric evolution, *J. geophys. Res.,* **114**(B5), doi:10.1029/2008JB005866.

Handy, M. R. 1990. The solid-state flow of polymineralic rocks, *J. geophys. Res.,* **95**(B6), 8647–8661.

Harris, R. A. 2017. Large earthquakes and creeping faults, *Rev. Geophys.,* **55**(1), 169–198.

Hayman, N. W. & Lavier, L. L. 2014. The geologic record of deep episodic tremor and slip, *Geology,* **42**(3), 195–198.

Hirth, G. & Guillot, S. 2013. Rheology and tectonic significance of serpentinite, *Elements,* **9**(2), 107–113.

Holdsworth, R. E. 2004. Weak faults - rotten cores, *Science,* **303**(5655), 181–182.

Ikari, M. J., Marone, C. & Saffer, D. M. 2011. On the relation between fault strength and frictional stability, *Geology,* **39**(1), 83–86.

Ikari, M. J., Marone, C., Saffer, D. M. & Kopf, A. J. 2013. Slip weakening as a mechanism for slow earthquakes, *Nat. Geosci.,* **6**(6), 468–472.

Im, K., Saffer, D., Marone, C. & Avouac, J. P. 2020. Slip-rate-dependent friction as a universal mechanism for slow slip events, *Nat. Geosci.,* **13**(10), 705–710.

Kaneko, Y., Avouac, J. P. & Lapusta, N. 2010. Towards inferring earthquake patterns from geodetic observations of interseismic coupling, *Nat. Geosci.,* **3**(5), 363–369.

Karner, S. L. & Marone, C. 2000. Effects of loading rate and normal stress on stress drop and stick-slip recurrence interval, in *Geocomplexity and the Physics of Earthquakes, 2000,* Vol. **120,** *Geophysical Monograph Series,* pp. 187–198, eds Turcotte, D.L., Klein, W. & Rundle, J.B., Blackwell Publishing Ltd.

Keller, J. V. A. & Pialli, G. 1990. Tectonics of the Island of Elba; a reappraisal, *Italian Journal of Geosciences,* **109**(), 413–425. https://pubs.geoscienceworld.org/italianjgeo/article/109/2/413/107462/Tectonics-of-the-Island-of-Elba-a-reappraisal.

Kostrov, B. V. 1974. Crack propagation at variable velocity. *J. Appl. Math. Mech.,* **38**(3), 511–519.

Kronenberg, A. K., Kirby, S. H. & Pinkston, J. 1990. Basal slip and mechanical anisotropy of biotite, *J. geophys. Res.,* **95**(B12), 19 257–19 278.

Leeman, J. R., Marone, C. & Saffer, D. M. 2018. Frictional mechanics of slow earthquakes, *J. geophys. Res.,* **123**(9), 7931–7949.

Leeman, J. R., Saffer, D. M. Scuderi, M. M. & Marone, C. 2016. Laboratory observations of slow earthquakes and the spectrum of tectonic fault slip modes, *Nature Communications, 7,1–6. https://doi.org/10.1038/ncomms11104,* **7,** 1–6.https://doi.org/10.1038/ncomms11104

Logan, J.M., 1979. Experimental studies of simulated gouge and their application to studies of natural fault zones, in *Proceedings of Conference VIII-Analysis of Actual Fault Zones in Bedrock,* pp. 305–343.

Mair, K., Frye, K. M. & Marone, C. 2002. Influence of grain characteristics on the friction of granular shear zones, *J. geophys. Res.,* **107**(B10), ECV 4–1-ECV 4-9.

Marone, C. 1998. Laboratory-derived friction laws and their application to seismic faulting, *Annu. Rev. Earth planet. Sci.,* **26**(1), 643–696.

Marone, C. & Richardson, E. 2010. Learning to read fault-slip behavior from fault-zone structure, *Geology,* **38**(8), 767–768.

McLaskey, G. C. 2019. Earthquake initiation from laboratory observations and implications for foreshocks, *J. geophys. Res.,* **124**(12), 12 882–12 904.

Mena, B., Martin Mai, P., Olsen, K. B., Purvance, M. D. & Brune, J. N. 2010. Hybrid broadband ground-motion simulation using scattering green's functions: application to large-magnitude events, *Bull. seism. Soc. Am.,* **100**(5 A), 2143–2162.

Moore, D. E. & Lockner, D. A. 2011. Frictional strengths of talc-serpentine and talc-quartz mixtures, *J. geophys. Res.,* **116**(1), 1–17.

Moore, D. E., Lockner, D. A. & Hickman, S. 2016. Hydrothermal frictional strengths of rock and mineral samples relevant to the creeping section of the San Andreas Fault, *J. Struct. Geol.,* **89,** 153–167.

Moore, D. E., Lockner, D. A., Ma, S., Summers, R. & Byerlee, J. D. 1997. Strengths of serpentinite gouges at elevated temperatures, *J. geophys. Res.,* **102**(B7), 14 787–14 801.

Moore, D. E., Lockner, D. A., Summers, R., Shengli, M. & Byerlee, J. D. 1996. Strength of chrysotile-serpentinite gouge under hydrothermal conditions: can it explain a weak San Andreas fault? *Geology,* **24**(11), 1041–1044.

Moore, D. E. & Rymer, M. J. 2007. Talc-bearing serpentinite and the creeping section of the San Andreas fault, *Nature,* **448**(7155), 795–797.

Niemeijer, A. R. & Spiers, C. J. 2007. A microphysical model for strong velocity weakening in phyllosilicate-bearing fault gouges, *J. geophys. Res.,* **112**(10), doi:10.1029/2007JB005008.

Niemeijer, A., Marone, C. & Elsworth, D. 2010. Fabric induced weakness of tectonic faults, *Geophys. Res. Lett.,* **37**(3), 1–5.

Okamoto, A. S., Verberne, B. A., Niemeijer, A. R., Takahashi, M., Shimizu, I., Ueda, T. & Spiers, C. J. 2019. Frictional properties of simulated chlorite gouge at hydrothermal conditions: implications for subduction megathrusts, *J. ggeophys. Res.,* **124**(5), 4545–4565.

Österle, W., Deutsch, C., Gradt, T., Orts-Gil, G., Schneider, T. & Dmitriev, A. I. 2014. Tribological screening tests for the selection of raw materials for automotive brake pad formulations, *Tribol. Int.,* **73,** 148–155.

Passelègue, F. X., Almakari, M., Dublanchet, P., Barras, F., Fortin, J. & Violay, M. 2020. Initial effective stress controls the nature of earthquakes, *Nat. Commun.,* **11**(1), 1–8.

Peng, Z. & Gomberg, J. 2010. An integrated perspective of the continuum between earthquakes and slow-slip phenomena, *Nat. Geosci.,* **3**(9), 599–607.

Pozzi, G., Scuderi, M. M., Tinti, E., Nazzari, M. & Collettini, C. 2022. The role of fault rock fabric in the dynamics of laboratory faults, *J. geophys. Res.,* **127**(6), doi:10.1029/2021JB023779.

Pranger, C., Sanan, P., May, D. A., Le Pourhiet, L. & Gabriel, A. A. 2022. Rate and state friction as a spatially regularized transient viscous flow law. *J. geophys. Res.,* **127**(6), 1–33.

Rabinowicz, E. 1951. The nature of the static and kinetic coefficients of friction, *J. appl. Phys.,* **22**(11), 1373–1379.

Reinen, L. A., Tullis, T. E. & Weeks, J. D. 1992. Two-mechanism model for frictional sliding of serpentinite, *Geophys. Res. Lett.,* **19**(15), 1535–1538.

Reinen, L. A., Weeks, J. D. & Tullis, T. E. 1994. The frictional behavior of lizardite and antigorite serpentinites: experiments, constitutive models, and implications for natural faults, *Pure appl. Geophys.,* **143**(3), 317–358.

Rice, J. R., 1983. Constitutive relations for fault slip and earthquake instabilities, *Pure and Applied Geophysics PAGEOPH,* **121**(), 443–475.https://doi.org/10.1007/BF02590151

Ruggieri, R. *et al.* 2021. The role of shale content and pore-water saturation on frictional properties of simulated carbonate faults, *Tectonophysics,* **807,** doi:10.1016/j.tecto.2021.228811.

Ruina, A. 1983. Slip instability and state variable friction laws, *J. geophys. Res.,* **88**(B12), 10 359–10 370.

Saffer, D. M. & Marone, C. 2003. Comparison of smectite- and illite-rich gouge frictional properties: application to the updip limit of the seismogenic zone along subduction megathrusts, *Earth planet. Sci. Lett.,* **215**(1–2), 219–235.

Saffer, D. M. & Wallace, L. M. 2015. The frictional, hydrologic, metamorphic and thermal habitat of shallow slow earthquakes, *Nat. Geosci.,* **8**(8), 594–600.

Schleicher, A. M., van der Pluijm, B. A. & Warr, L. N. 2010. Nanocoatings of clay and creep of the San Andreas fault at Parkfield, California. *Geology,* **38**(7), 667–670.

Schneider, C. A., Rasband, W. S. & Eliceiri, K. W. 2012. NIH Image to ImageJ: 25 years of image analysis, *Nat. Methods,* **9,** 7, 671–675.

Scholz, C. H. 2019. The mechanics of earthquakes and faulting, in *The Mechanics of Earthquakes and Faulting,* Cambridge Univ. Press.

Scholz, C., Molnar, P. & Johnson, T. 1972. Detailed studies of frictional sliding of granite and implications for the earthquake mechanism, *J. geophys. Res.,* **77**(32), 6392–6406.

Scuderi, M. M. & Carpenter, B. M. 2022. Frictional stability and hydromechanical coupling of serpentinite-bearing fault gouge. *Geophys. J. Int.,* **231**(1), 290–305.

Scuderi, M. M., Marone, C., Tinti, E., Di Stefano, G. & Collettini, C. 2016. Precursory changes in seismic velocity for the spectrum of earthquake failure modes, *Nat. Geosci.,* **9**(9), 695–700.

Scuderi, M. M., Tinti, E., Cocco, M. & Collettini, C. 2020. The role of shear fabric in controlling breakdown processes during laboratory slow-slip events, *J. geophys. Res.,* **125**(11), 1–23.

Sibson, R. H., 1977. Fault rocks and fault mechanisms, *Journal of the Geological Society,* **133**(), 191–213. https://doi.org/10.1144/gsjgs.133.3.0191.

Skarbek, R. M., Rempel, A. W. & Schmidt, D. A. 2012. Geologic heterogeneity can produce aseismic slip transients, *Geophys. Res. Lett.,* **39**(21), 1–5.

Tarling, M. S., Smith, S. A. F. & Scott, J. M. 2019. Fluid overpressure from chemical reactions in serpentinite within the source region of deep episodic tremor, *Nat. Geosci.,* **12**(12), 1034–1042.

Tarling, M. S., Smith, S. A. F., Viti, C. & Scott, J. M. 2018. Dynamic earthquake rupture preserved in a creeping serpentinite shear zone, *Nat. Commun.,* **9**(1), doi:10.1038/s41467-018-05965-0.

Tembe, S., Lockner, D. A. & Wong, T.-F. 2010. Effect of clay content and mineralogy on frictional sliding behavior of simulated gouges: binary and ternary mixtures of quartz, illite, and montmorillonite, *J. geophys. Res.,* **115**(B3), doi:10.1029/2009JB006383.

Tesei, T., Collettini, C., Barchi, M. R., Carpenter, B. M. & Di Stefano, G. 2014. Heterogeneous strength and fault zone complexity of carbonate-bearing thrusts with possible implications for seismicity, *Earth planet. Sci. Lett.,* **408,** 307–318.

Tesei, T., Collettini, C., Carpenter, B. M., Viti, C. & Marone, C. 2012. Frictional strength and healing behavior of phyllosilicate-rich faults, *J. geophys. Res.,* **117**(9), 1–13.

Tesei, T., Harbord, C. W. A., De Paola, N., Collettini, C. & Viti, C. 2018. Friction of mineralogically controlled serpentinites and implications for fault weakness, *J. geophys. Res.,* **123**(8), 6976–6991.

Tinti, E., Spudich, P. & Cocco, M. 2005. Earthquake fracture energy inferred from kinematic rupture models on extended faults, *J. geophys. Res.,* **110**(12), 1–25.

van den Ende, M. P. A., Chen, J., Ampuero, J. P. & Niemeijer, A. R. 2018. A comparison between rate-and-state friction and microphysical models, based on numerical simulations of fault slip. *Tectonophysics,* **733,** 273–295.

Vannucchi, P. 2019. Scaly fabric and slip within fault zones. *Geosphere,* **15**(2), 342–356.

Viti, C., Collettini, C., Tesei, T., Tarling, M. S. & Smith, S. A. F. 2018. Deformation processes, textural evolution and weakening in retrograde serpentinites, *Minerals,* **8**(6), doi:10.3390/min8060241.

Volpe, G. *et al.* 2022a. Frictional controls on the seismogenic zone: insights from the Apenninic basement, Central Italy, *Earth planet. Sci. Lett.,* **583,** doi:10.1016/j.epsl.2022.117444.

Volpe, G., Pozzi, G. & Collettini, C. 2022b. Y-B-P-R or S-C-C′? Suggestion for the nomenclature of experimental brittle fault fabric in phyllosilicate-granular mixtures, *J. Struct. Geol.,* **165,** doi:10.1016/j.jsg.2022.104743.

Wintsch, R. P., Christoffersen, R. & Kronenberg, A. K. 1995. Fluid-rock reaction weakening of fault zones, *J. geophys. Res.,* **100**(B7), 13 021–13 032.

Xing, T., Zhu, W., French, M. & Belzer, B. 2019. Stabilizing effect of high pore fluid pressure on slip behaviors of gouge-bearing faults, *J. geophys. Res.,* **124**(9), 9526–9545.

Yoffe, E. H. 1951. The moving Griffith crack. *Phil. Mag.,* **42**(330), 739–750.